

Analysis of the plasma response in a 5kW class HET from a 2Dzr PIC model

A. Marín-Cebrián,¹ E. Ahedo,¹ and A. Domínguez-Vázquez²

¹⁾Department of Aerospace Engineering, Universidad Carlos III de Madrid, Leganés, Spain

²⁾Department of Fluid Mechanics, Universidad de Málaga, Málaga, Spain

(*Electronic mail: almarinc@pa.uc3m.es)

(Dated: 29 January 2025)

A two-dimensional particle-in-cell model has been applied to simulate axial-radial plasma response in a virtual 5kW Hall thruster which resembles the PPS®5000. The time evolution of plasma currents to the domain boundaries shows convergence and the time-averaged steady-state solution is analyzed. The plasma response is strongly affected by the complex magnetic field topology. The curved magnetic field near the anode effectively inhibits the radial plasma motion, reducing particle and energy losses to the walls. The simulation results suggest that the Debye sheaths at the lateral dielectric walls may collapse for a grazing magnetic field incidence angle. The analysis of the radial electron momentum equation reveals a balance between the pressure gradient, electric and magnetic forces. The dominant terms in such equation change depending on the magnetic field curvature. Near the exit, the magnetic field is almost radial and the pressure gradient and electric force approximately balance each other. Near the anode, the magnetic field is curved towards the anode and the dominant terms in the equation are the pressure and magnetic forces. The radial magnetic force depends on the azimuthal electron current, which is found to be a combination of $\mathbf{E} \times \mathbf{B}$ and diamagnetic drifts. The azimuthal momentum balance, which determines the axial electron current, reveals that Finite-Larmor-Radius effects become important near the anode.

I. INTRODUCTION

Currently, a large part of Hall Effect Thruster (HET) numerical research relies on 2D axial-radial (2Dzr) hybrid models^{1,2}, treating heavy species (i.e. ions and neutrals) with a particle-in-cell (PIC) formulation and electrons as a drift-diffusive fluid. EA: esta afirmación tan fuerte necesita de más referencias que 2, o reformular la frase The standard macroscopic formulation for electrons is based on the assumption that their velocity distribution function (VDF) is (near) Maxwellian³. However, the low collisionality in the HET channel prevents the plasma from reaching local thermodynamic equilibrium; and thus, standard fluid models can misrepresent some relevant physics⁴. Alternatively, kinetic models do not make any assumptions on the VDF shape; but the wide range of time and length scales that need to be resolved make multidimensional simulations challenging⁵.

Recently, we have developed the 2D PIC model PICASO^{6,7} to analyze the kinetic response of the HET plasma. In a previous work⁷, we applied this model to simulate the axial-radial plasma dynamics in a simplified HET configuration with a perfectly radial magnetic field. The analysis focused mainly on the electron response and the kinetic solution revealed important differences with respect to standard fluid models: (1) plasma-wall interaction parameters can differ largely from classical theory, based on a Maxwellian VDF, (2) the electron heat flux has a complex behavior and, in general, it cannot be described by a Fourier-type law, and (3) the pressure tensor is composed of a gyrotropic anisotropic part and small gyroviscous terms. Indeed, near the anode, gyrovis-

cosity and inertia are relevant in the azimuthal electron momentum equation, where dominant terms are two orders of magnitude smaller than in the axial momentum equation.

However, the magnetic field topology in HETs is curved. EA: con diferentes configuraciones en distintos prototipos (lente magnético, a pantalla miento magnético, puntos nulos cerca de ánodo, etc.) Experimental^{8,9} and numerical^{10,11} AM: revisar citas EA: el artículo de miedzik no puede ir aquí? works, have shown that oblique magnetic fields can reduce plasma fluxes to the walls and enhance the thruster performances. EA: alternativa: in ref.¹², a 1D radial (1Dr) PIC model showed, first, a significant reduction in electron anisotropy when the magnetic field is moderately-curved magnetic field and, second, a reduction of the plasma fluxes to the radial walls when la componente magnética radial es confinante. (que añade nuestro trabajo numérico a los anteriores?) In one of our previous works¹², we used a 1D radial (1Dr) PIC model to investigate the effect of a moderately-curved magnetic field in the radial plasma behavior. The kinetic solution showed a significant reduction in electron anisotropy, in agreement with Ref. 13. A magnetic force term, which can be electron confining or expanding, appears in the radial momentum equation and modifies the relative relevance of the radial pressure gradient and electric force density. As a consequence, the plasma density near the wall and the degree of radial ion defocusing were affected. However, such study was limited by the intrinsic shortcomings of a 1Dr model. A consistent analysis of the impact of the magnetic field topology requires a 2Dzr model of the

discharge.

In this work we extend the model of Ref. 7 to afford the simulation of more realistic configurations, including a complex magnetic topology. **EA: menciona algo más que lo haga realista AM: cylindrical effects on the calculation of the fields and particle mover and elastic, excitation and ionization e-n collisions with cross sections extracted from the LxCat database.** The simulated scenario takes the inputs of a virtual 5kW Hall thruster which resembles the PPS®5000 **EA: aquí tienes que dar alguna referencia del motor real y quizás citar domi22a** and the analysis focuses on the steady-state plasma response. The effect of the curved magnetic field on the macroscopic plasma response and plasma-wall interaction magnitudes are discussed. The analysis of the electron momentum equation explains some aspects of the macroscopic plasma response and reveals the important terms along the axial, radial and azimuthal directions. **EA: creo que este párrafo le falta algunas cosas para justificar mejor este trabajo**

The article is structured as follows. Section II summarizes the main aspects of the kinetic model. Section III presents and analyzes the simulation results for the proposed scenario. Macroscopic plasma magnitudes, wall interaction parameters and the electron momentum equation satisfied by the kinetic electrons are under scrutiny. Finally, conclusions are gathered in Section VII. Preliminary results of this work were presented at the 38th International Electric Propulsion Conference¹⁴.

II. THE KINETIC MODEL

The axisymmetric (i.e. $\partial/\partial\theta = 0$) 2Dzr PIC model, PICASO, aims to solve the plasma response in a Hall thruster discharge. This Section summarizes the the main features of the kinetic code. The main input parameters for the model are gathered in Table I.

Figure 1 provides a sketch of the simulation domain, comprising the thruster channel and a small portion of the near plume. The domain boundaries are defined by the a metallic anode (A), the dielectric thruster walls (W), and the downstream plume boundary which acts as the cathode/neutralizer (N). The thruster has dimensions $L = 29$ mm, $r_{W1} = 54.5$ mm and $r_{W2} = 76.7$ mm for the channel length, inner and outer radii respectively. The simulation domain extends from $z \in [0, 87]$ mm (equivalent to three channel lengths) and $r \in [34.5, 96.7]$ mm (almost three times the channel width).

Electrons, e , and singly charged xenon ions, i , are simulated as two different populations of macroparticles with constant weight (i.e. number of elementary particles per simulated macroparticle). Explicit time integration of particle trajectories is performed using the Boris algorithm¹⁵ and cylindrical effects on the particle motion are accounted for as described in Ref. 16. First-order weighting schemes (Cloud-In-Cell) are used

for both, interpolating \mathbf{B} and \mathbf{E} to the particle position, and calculating integral moments of each species VDF (i.e. the macroscopic magnitudes) at the mesh nodes. Electron and ion particles reaching any of the domain boundaries contribute to the electric current to that surface and then removed from the simulation. Secondary electrons are emitted by the dielectric walls following a linear SEE yield law, $\delta_s(\mathcal{E}_{eWt}) = \mathcal{E}_{eWt}/\mathcal{E}_c$, with \mathcal{E}_{eWt} the impacting electron energy and $\mathcal{E}_c = 50$ eV the material cross-over energy. Secondary electrons are sampled from a Maxwellian flux VDF with an average energy of 0.4 eV. Additionally, electrons are injected from the cathode such that continuity of discharge current, I_d , is satisfied at any instant of the simulation. Electrons generated at the cathode are sampled from a Maxwellian flux VDF with a mean energy of 4.5 eV and the injected flux distribution over the neutralizer boundary is assumed uniform.

Neutrals, n , are described as a background fluid and follow a simplified depletion law; which avoids simulating long time-scales associated to the slow neutral dynamics. It cancels breathing mode oscillations and allows reaching steady-state solutions of the discharge, as shown in Ref. 7. In the thruster channel, the axially dependent neutral density $n_n(z)$ is calculated as

$$n_n(z) = \frac{\dot{m} - \dot{m}_{zi}}{u_{zn} A m_i}, \quad (1)$$

where m_i is the ion mass, A is the channel cross section area, $u_{zn} = 300$ m/s is the (constant) neutral axial fluid velocity, \dot{m}_{zi} is the axial ion mass flow and $\dot{m} = 17.59$ mg/s is the injected neutral mass flow at the back wall. Equation (1) conserves the total mass flow and accounts for both, volumetric ionization and recombination of ions reaching the thruster walls. In the near plume, n_n is assumed constant.

Collisions include include elastic, excitation and ionization e - n events, while ions are considered collisionless. The collisional cross-sections are retrieved from the Biagi database¹⁷ available in LxCat. Ideally, all excitation collisions should be implemented in the simulation code. However, in order to make simulations computationally lighter, it is convenient to define an effective excitation collision which groups the effect of all these processes. In this simulation, an equivalent excitation event with an energy loss $\Delta\mathcal{E}_{exc} = -10$ eV is considered.

Due to the axial-radial nature of the simulation, azimuthal instabilities inducing cross-field electron transport cannot be resolved. Alternatively, an empirical model is used, and their effect is included as an isotropic anomalous collisionality of the form $\nu_{ano} = \alpha_{ano}\omega_{ce}$, with $\omega_{ce} = eB/m_e$ the electron cyclotron frequency and α_{ano} a fitting function. Here, the anomalous transport map of Ref. 18, calibrated to reproduce typical values of the PPS5000, has been applied.

The magnetic field, \mathbf{B} , is static and externally applied. The 2D map of the imposed magnetic topology is shown in Fig. 2(a), including the field magnitude and contours for the magnetic field lines. As it can be ob-

served, the magnetic field is radially asymmetric. The topology is almost radial near the channel exit but features a large curvature in the inner part of the channel. We can distinguish between magnetic field lines connecting the two lateral walls (with a moderate curvature) and those joining one of the lateral walls with the anode (with large curvature). The magnetic separatrix that depicts the approximate transition between these two regions is plotted in red in Fig. 2(a). It intersects the inner wall at $z \approx 8.46$ mm, the outer wall at $z \approx 13.65$ mm, and the anode wall at $r \approx 62.9$ mm, bounding the region of strong magnetic field curvature. Additionally, the intersection of the magnetic separatrix with the anode surface also coincides with a point where the magnetic field becomes practically null, $\min(B_A) \approx 0.2$ G. Axial profiles of the magnetic field norm along the mean radius, and at $r = 62.9$ mm are plotted for comparison in Fig 2(b).

In the electrostatic approximation the electric field is $\mathbf{E} = -\nabla\phi$ and the electric potential, ϕ , is obtained from the Poisson equation

$$\frac{\partial^2\phi}{\partial z^2} + \frac{\partial^2\phi}{\partial r^2} + \frac{1}{r} \frac{\partial\phi}{\partial r} = \frac{e(n_e - n_i)}{\epsilon}, \quad (2)$$

where ϵ is the electric permittivity and n_e , n_i are the electron and singly charged ion densities respectively. Dirichlet boundary conditions are imposed at the anode ($\phi_A = 300$ V) and cathode surfaces ($\phi_N = 0$), fixing the discharge potential $V_d = \phi_A - \phi_N$, and Neumann conditions are applied at the dielectric walls. The numerical implementation makes use of finite differences for the calculation of ϕ and \mathbf{E} at the mesh nodes.

The strict numerical constraints on the cell size and time step imposed by the Debye length and the inverse plasma frequency respectively are relaxed by using an augmented permittivity $\epsilon = f_D^2 \epsilon_0$, where ϵ_0 is the vacuum permittivity. This allows a reduction of a factor f_D^3 in computational cost without a significant distortion of the steady-state solution as long as the Debye length remains the smallest length scale of the problem⁷. For the simulations shown here we apply $f_D = 12$, a common value used in previous works in the literature^{11,19}.

Regarding numerical parameters, a square mesh with cell size $\Delta z = \Delta r = 200$ μm has been employed **EA: relacionar estos tamaños con fD=12 y la longitud Debye aumentada? AM: Tabla I, fD = 12 yields a characteristic Debye length } \lambda_{De} = 230 \mu\text{m and inverse plasma frequency } \omega_{pe}^{-1} = 123 \text{ ps}**. The simulation time-step is $\Delta t = 15$ ps and the total simulated time is 60 μs . The simulation shown here was run using 20 cores on a workstation with 2 sockets, each one with 20 cores Intel(R) Xeon(R) Gold 6230 CPU @ 2.10 GHz. The simulation time is approximately one week.

III. SIMULATION RESULTS AND DISCUSSION

A. Transient response

The simulation starts with a filled domain and Maxwellian VDFs for electrons and ions. Initially, identical particle densities and temperatures for electrons and ions are considered, with $n_{e0} = n_{i0} = 4 \cdot 10^{17} \text{ m}^{-3}$ and $T_{e0} = T_{i0} = 1 \text{ eV}$. The time evolution of electron and ion currents to different boundary surfaces exhibit oscillations with a period of some μs , which corresponds with time-scales of the ion dynamics. Such oscillations are stronger initially but are damped over time. To illustrate this behavior, the currents to the outer wall are plotted in Fig. 3. After approximately 40 μs , steady-state is reached. Hereon, only the stationary plasma response will be discussed. In order to mitigate the PIC related noise, stationary results are time-averaged over the last 7.5 μs of the simulation (i.e. 500000 time-steps). At steady-state, the number of simulated particles per species is over one million.

Table II gathers the integrated current and energy deposited at different important thruster surfaces at steady-state. The discharge current is $I_d \approx 18 \text{ A}$, which yields a discharge power of $P_d \approx 5.5 \text{ kW}$. Those figures agree well with the expected operation of a 5kW-class HET that we are aiming to simulate.

B. Description of the stationary response

The 2D maps of relevant macroscopic magnitudes are shown in Fig. 4: (a) electric potential, ϕ ; (b) electron temperature, T_e ; (c) electron density, n_e ; (d) azimuthal electron current, $j_{\theta e}$; (e) and (f) longitudinal ion and electron current densities respectively. For a given vector magnitude, the longitudinal part is defined as $\tilde{\Gamma} = \Gamma - \Gamma_\theta \mathbf{1}_\theta$. In this paper, the analysis focuses on the HET channel, while the boundary conditions at the near plume only provide a closure to the discharge. Non-neutral Debye sheaths develop in the vicinity of material surfaces but most of the plasma remains quasineutral. Although factor f_D thickens the sheaths (about 12 times), they still cover a rather small portion of the domain. The analysis of the local plasma behavior within the channel reveals significant differences between the near-anode and near-exit regions. The magnetic separatrix acts as a boundary between these two plasma regions. In the near-exit region, where the magnetic field is almost radial, the macroscopic plasma response follows the known trends from 1Dz/1Dr fluid models²⁰. However, in the near-anode region, the plasma features a complex 2D response due to the large magnetic field curvature. This motivates a deeper analysis of this region in Section VI.

The electron energy flux vector ($\mathbf{P}_e'' = m_e/2 \iiint v^2 v f_e d^3 v$) can be expressed as the addition of

four different contributions

$$\mathbf{P}_e'' = \mathbf{h}_e + \mathbf{q}_e + \mathbf{U}_e + \mathbf{\Pi}_e, \quad (3)$$

with $\mathbf{h}_e = (5/2)n_e T_e \mathbf{u}_e$ the enthalpy flux, \mathbf{q}_e the heat flux, $\mathbf{U}_e = m_e u_e^2 n_e \mathbf{u}_e / 2$ the flux of fluid flow energy and $\mathbf{\Pi}_e = (\bar{\rho}_e - p_e \bar{I}) \cdot \mathbf{u}_e$ the term caused by the fact that the electron pressure tensor deviates from an isotropic gyrotropic one. The different terms in Eq. (3) are plotted in Fig. 6 (a), (b), (c) and (d) respectively. The electron energy flux vector follows complex 2D patterns. In most of the channel, the enthalpy and heat flux clearly dominate. However, \mathbf{U}_e and $\mathbf{\Pi}_e$ become relevant near the anode surface since in this region the azimuthal fluid electron velocity can become comparable to the electron thermal speed, c_e .

C. Radial profiles

Figure 7 plots profiles of electric potential, plasma density and electron temperature at five different axial locations. For a better comparison, density and potential profiles are presented in non-dimensional form, $n_{i,e}/\bar{n}_e$ and $e(\phi - \phi_M)/\bar{T}_e$, where M refers to the mean channel radius $r_M = (r_{W1} + r_{W2})/2$ and a bar over a magnitude indicates that it is a radially averaged value, i.e. $\bar{G}(z) = (r_2^2 - r_1^2)^{-1} \int_{r_1}^{r_2} 2r G(z, r) dr$. Macroscopic magnitudes exhibit radial asymmetries that become more noticeable in sections closer to the anode and can be mainly attributed to the imposed magnetic topology. Radial profiles at $z = 1.5, 2.5$ cm have a common behavior and resemble those obtained with a 1Dr PIC model of the discharge assuming a purely radial magnetic field^{21,22}. However, for $z < 1.0$ cm, the potential profile does not decrease monotonically towards the walls and the plasma density is concentrated at $r = 6.29$ cm. These radial profile of n_e follow the same qualitative trends as in Ref. 12 for magnetic lenses with a large curvature towards the anode. The large axial component of the magnetic field near the anode strongly inhibits radial plasma flows. A novelty of the results shown here is that the simulation suggests that the lateral wall Debye sheaths may collapse for a grazing magnetic incidence. The plasma response in near-anode region is further discussed in Section VI.

D. Velocity distribution functions

The PIC model implementation allows to calculate velocity distribution functions of electrons and ions at different locations.

Figure 9 plots the normalized 1V electron VDFs⁷ at $r = 6.29$ cm and different axial positions, which corresponds to the axial locations selected in Fig. 7. The VDFs are plotted in logarithmic scale in the 'y' axis and the 'x' axis represents the directional electron energy

$m_e v_{xe} |v_{xe}| / 2$, for $x = z, r, \theta$. Therefore, a Maxwellian VDF yields a line with constant slope. The wider the VDF (larger velocity dispersion), the higher the temperature. The relative shapes of the VDFs in Fig. 9 show that the peak electron temperatures are reached near the thruster exit, in agreement with Fig. 4(b). At $z = 1.5$ cm and $z = 2.5$ cm the axial and azimuthal VDF are almost identical with an approximately linear slope, yielding $T_{ze} \approx T_{\theta e}$. The weak asymmetry between $\hat{f}_e^{(z)}$ and $\hat{f}_e^{(\theta)}$ is due to $u_{ze} < u_{\theta e} \ll c_e$. Along the radial direction, the VDF is depleted beyond a certain energy threshold, since electrons with high radial energies are collected by the walls. This reduces the radial temperature and leads to anisotropy with $T_{re} < T_{ze} \approx T_{\theta e}$. This result is identical to those obtained from previous 1Dr models of the acceleration region of the discharge assuming a purely radial magnetic field^{21–23}. As we move towards the central part of the channel the magnetic curvature increases. At $z = 0.9$ cm there is a large replenishment of the radial VDF and at $z = 0.6$ cm there is no visible effect of the radial wall losses, leading to a rather isotropic electron temperature $T_{re} \approx T_{ze} \approx T_{\theta e} \approx T_e$. This result is analogous to previous works with 1D models accounting for the magnetic field curvature^{12,13}, which explained this effect due to the larger mixing between the radial and axial components of the velocity as a consequence of the magnetic field shape. The larger asymmetry between $\hat{f}_e^{(\theta)}$ and $\hat{f}_e^{(z)}, \hat{f}_e^{(r)}$ is the signature of a greater $u_{\theta e}$. Closer to the anode, at $z = 0.3$, an asymmetry in the axial VDF can be observed, with more electrons traveling with $v_z < 0$ than in the opposite direction. This is a consequence of the collection of electrons by the anode wall, as previously observed in Ref. 7, which leads to a lower T_{ze} . 1D models are not suitable to analyze this region.

AM: Comentario sobre las VDFs de iones. Figure 24 depicts the VDF of ions. As expected, the peak of the axial ion VDF moves towards the higher positive energies as ions are accelerated downstream. Moreover, the VDF shows dispersion in ion velocities. Interpreting such dispersion in terms of temperature can be misleading since their VDF differs much from a Maxwellian. This is indeed expected since ions are collisionless. **AM: The peak of low energy ions at $r = 6.29$ cm and $z = 1.5$ cm is due to ionization. It is consistent with the shape of $u_{zi}(z)$, in figs/axial_profiles_ref.png**

IV. MACROSCOPIC BALANCES

A. The electron momentum equation

The radial response is determined by the radial momentum equation. The dominant contributions to this equation are

$$0 \approx -\frac{\partial p_{rre}}{\partial r} - e n_e E_r + j_{\theta e} B_z. \quad (4)$$

Therefore, it reduces to a balance among the electron pressure, electric and magnetic force. The different terms in this equation are plotted in Fig. 15 at five axial sections of the HET channel. In each axial section the electric and pressure forces change sign. Thus, the electric force is an electron confining force (pushing the electron fluid away from the walls) and the electron pressure is an electron expanding force (pushing the electron fluid towards the walls). The magnetic force can be electron expanding or confining depending on the magnetic field curvature. For a magnetic field curved towards the anode the magnetic force has a confining character while in the opposite configuration the magnetic force has an electron expanding character¹².

Near the anode the electron-confining magnetic force is compensated by the electron pressure term and the electric force term remains small. This justifies the smooth gradients of the electric potential, an electron density that presents sharp changes and is concentrated away from the walls [see Fig. 7(a) and (b) for $z < 1.0$ cm]. As the curvature of the magnetic field decreases in the thruster channel B_z becomes smaller and the magnetic term in the radial momentum equation becomes less relevant. As a consequence, the radial momentum equation approximately simplifies to a balance between the expanding pressure force and the confining electric force. Finally, it is worth noting that at $z = 2.5$ cm the magnetic force does not change sign inside the channel and it is always pushing the electron fluid towards the inner wall. **AM: This leads to higher particle fluxes to the inner wall than to the outer wall.**

As it has been shown, the term $j_{\theta e}B_z$ has a key role in the radial plasma response. The azimuthal electron current, $j_{\theta e}$, is determined by the axial momentum equation

$$0 \simeq -\frac{\partial p_{zze}}{\partial z} - en_e E_z - j_{\theta e} B_r. \quad (5)$$

The radially averaged contributions to Eq. (5) are plotted in Fig. 16(a). Collisional effects and M_{rze} leave a negligible contribution to the equation. The effect of electron inertia is small and it is only noticeable at the anode sheath. Therefore, the solution of this equation is quite standard, with an azimuthal electron velocity which is a combination of $\mathbf{E} \times \mathbf{B}$ and diamagnetic drifts. The $\mathbf{E} \times \mathbf{B}$ term dominates near the exit while the diamagnetic term is more important near the anode. The local maxima in the electric and magnetic force contributions are due to the local features of the plasma response in the near anode region, to be analyzed in more detail in the Section VI.

The azimuthal electron momentum equation determines the axial electron current towards the anode. The main terms involved in this balance are

$$0 \simeq -\frac{\partial M_{z\theta e}}{\partial z} + j_{ze} B_r - j_{re} B_z + F_{col,\theta e}. \quad (6)$$

The radially averaged contributions to Eq. (6) are plotted in Fig. 16(b). Here, the dominant terms are much

smaller (typically 2 orders of magnitude) than in the axial momentum equations. Near the thruster exit B_z is small and $\partial M_{z\theta e}/\partial z$ leaves a negligible contribution to the balance, i.e. $j_{ze} B_r \simeq -F_{col,\theta e}$. Conversely, near the anode, all the terms in the Eq. (6) are relevant. The result obtained here highlight the key role of Finite-Larmor-Radius (FLR) effects near the anode, as already found by previous kinetic models^{7,24,25}.

AM: Decidir si mantenemos algo de esto.

One may argue that this result is affected by the empirical treatment of anomalous transport. However, previous works with a 2Dzθ PIC model of a HET discharge²⁴, self-consistently resolving the azimuthal plasma instabilities, also found a similar result (however, they believed it was a numerical artifact due to the lack of collisions in the simulation). Many different kinetic simulations^{7,24,25}, seem to point towards the key role of FLR effects in the azimuthal momentum balance near the anode. **EA: ya lo hemos dicho en el artículo anterior creo** Nonetheless, we do not claim that this behavior is universal in HET physics. Whether FLR dominates over classical collisions and anomalous diffusion depends on the neutral density and local plasma properties. Fig. 17 plots the radially averaged collision frequencies in the current simulation. **EA: creo que este párrafo hay que replantearlo**

B. Continuity equation

EA: este estudio ya lo hiciste en el artículo anterior, qué hay de nuevo aquí que haya que resaltar? AM: Se puede eliminar

The radially integrated steady-state current balance for electrons and ions can be expressed as

$$\frac{dI_{zs}}{dz} = \frac{dI_{prod}}{dz} - \frac{dI_{rs}}{dz}, \quad s = i, e, \quad (7)$$

with I_{zs} the axial current, dI_{prod}/dz the rate of current production, and dI_{rs}/dz the rate of current losses to the lateral walls. Figure 14(a) plots the different contributions to this balance. Near the anode, the plasma losses to the walls are very small; therefore, all the plasma production due to ionization contributes to the axial current. Conversely, near the thruster exit ionization compensates plasma losses to the lateral walls.

AM: Decidir qué queremos contar sobre v_{wall} . Wall losses increase progressively from the anode to the thruster exit. Previous 1Dz models^{26,27} describe wall losses as

$$\frac{1}{A} \frac{dI_{rs}}{dz} = e \bar{n}_e v_w, \quad (8)$$

with \bar{n}_e the average plasma density in the cross section and v_w the wall collision frequency, defined as²⁶

$$v_w = \tilde{v}_w \frac{2\pi R}{A} \bar{c}_s, \quad (9)$$

with R the mean channel radius, $\bar{c}_s = \sqrt{T_e/m_i}$ the radially averaged sonic speed for ions and \tilde{v}_w is a phenomenological parameter to be fitted. In Ref. 20, based on a radial model of the discharge, Ahedo and Gallardo estimated $\tilde{v}_w \in [0.7, 1.2]$ for typical discharge parameters. However, a parametric analysis on the effect of this magnitude on the 1Dz fluid model led them to conclude that in fact $\tilde{v}_w \in [0.15, 0.25]$ in order to reproduce reasonably experimental data. Indeed, subsequent studies^{26,27} with improved versions of this model consider $\tilde{v}_w = 0.17$. **EA:** la versión está mejorada pero no precisamente en esto, que viene heredado de Escobar creo. Te sobra buena parte de la discusión anterior. Solo hay que decir que es un parámetro fenomenológico y que los modelos lo suponen constante en Z, así que es un valor promedio axial. This low value of \tilde{v}_w is difficult to justify using simplified 1D radial models and physically it represents a strong inhibition of the radial plasma fluxes. **EA:** creo que guitaría esta frase.

EA: lo importante es que nuestra solución ahora nos da el valor local que tiene y que resultaba variar mucho a lo largo de Z, bla bla bla
The kinetic model results in Fig. 14(b) suggest that $\tilde{v}_w \sim O(1)$, in agreement with the estimations from 1Dr models, near the thruster exit, where the magnetic field is approximately radial. However, close to the anode, where the magnetic field has a strong curvature and becomes almost parallel to the walls, this value is reduced between one and two orders of magnitude. It seems clear that the value of \tilde{v}_w is strongly affected by the magnetic field topology and it is the magnetic field that is responsible for inhibiting plasma fluxes to the walls.

EA: si buscásemos el valor medio de ese parámetro, que no saldría? Otra posibilidad es aproximarla por 0 en una región y por 1 en la otra

V. PLASMA-WALL INTERACTION

Figure 12(a) shows the local distribution of ion and electron current densities to the metallic anode wall. The radial position where particle fluxes to the anode are maxima coincides with the location where the magnetic separatrix touches the anode. This is consequence of the local plasma response near the anode, to be commented in Section VI. The integrated values in Table II show that the ion current collected by the anode is approximately a 1.5% of the electron current flowing to that boundary, $I_{iA} \approx 0.29$ A and $I_{eA} \approx 18.71$ A. In normal operation it is desirable that the anode current is dominated by electrons; however, some ions must reach the anode surface to avoid bad plasma attachment and sheath reversal²⁸. Standard theory predicts that no sheath develops for $|I_{iA}|/|I_{eA}| \leq 0.5\%$ for singly charged cold xenon ions²⁹
EA: este resultado es para un campo radial, yo lo pondría aquí **AM:** Creo que en el cálculo de este

resultado la forma del campo magnético es irrelevante mientras la longitud de Debye sea mucho menor que el radio de Larmor. Este resultado viene de la teoría clásica de vainas no magnetizadas. The PIC model provides a potential difference between the anode wall and sheath edge (defined at the location where the axial ion velocity towards the anode becomes sonic, i.e. $-u_{zi} = \sqrt{T_e/m_i}$) of only a few Volts. This justifies the low average ion impact energy to the anode $\mathcal{E}_{iA} \approx 6$ eV. Electrons reach the anode with a higher average energy $\mathcal{E}_{eA} \approx 20$ eV. This is a consequence of the local features of the electron VDF [see Fig. 9(a), which presents an asymmetric VDF along the axial direction. **AM:** Axial VDFs at $z = 0.3$ cm and other radial location, in Fig. 23, shows different slopes for high energy and low energy electrons which explains why the electrom impact energy is relatively constant along r but the temperature changes.] and inertia.

The inner and outer lateral walls present asymmetries in the current and power deposition figures. In particular, we observe higher electron and ion currents to the inner wall although the outer wall has larger surface area (the relation between the inner and outer wall surface areas is $r_{W2}/r_{W1} \approx 1.41$). This is consistent with the electron density map in Fig. 4(c) and the radial profiles of electron density shown in Fig. 7(b), which show consistently higher densities near the lower wall. Which, in turn, is due to the radially asymmetric magnetic topology. On the contrary, we find a higher emission of secondary electrons from the outer wall. In absolute terms, the current of SEE generated at the lateral walls are $|I_{eW1f}| = 4.04$ A and $|I_{eW2f}| = 4.62$ A. In relative terms, the ratio between the current of secondary electrons emitted by the wall with respect to the current of electrons reaching the wall yields $\delta_{s1} \approx 0.52$ and $\delta_{s2} \approx 0.71$. This means that the average energy of electrons reaching the outer wall is higher than those collected at the inner wall. **EA:** logramos explicar por qué? **AM:** Es consistente con los valores locales de la energía de impacto, mapas de temperatura e inercia de electrones. No sé si hace falta dar una explicación más rigurosa. This results in a higher electron power deposition at the outer wall. SEE from the dielectric walls promotes power losses to the walls, since secondary electrons are much colder than electrons reaching the thruster walls.

Local wall interaction magnitudes along the inner and outer dielectric walls are depicted in Fig. 13. From Fig. 13(a) and (b) it can be confirmed that, at steady state, the dielectric walls are locally current free. Therefore, the net axial electric current must be conserved at every axial section of the thruster channel, which has been checked to be well satisfied by the kinetic solution. The amount of particles reaching the lateral walls in the region bounded by the anode and the magnetic separatrix can be several orders of magnitude smaller than in the rest of the channel. However, the electrons that are capable to reach the walls are more energetic, which is trans-

lated into a local increase in the electron impact energy. This, in turn, leads to higher fraction of SEE. The energy flux, that combines information of the particle flux and energy, still decreases since the moderate increase in electron energies cannot compensate the sharp decrease in fluxes to the walls.

VI. ANALYSIS OF THE NEAR-ANODE REGION

Figure 10 zooms in the region that extends from the anode to $z = 1.5$ cm, which comprises the region with large magnetic field curvature near the anode and the progressive transition to a near-radial magnetic field in the acceleration region of the thruster. It can be observed that all the macroscopic variables in this region are strongly affected by the magnetic field shape. Indeed, the magnetic separatrix coincides with changes in trends of the main plasma parameters.

Electrons cannot easily cross the magnetic separatrix. This leads to a region with a very small plasma density. The electron and ion densities, shown in Fig. 10(a) and (b) respectively, shape the electric potential and electric field maps, depicted in Fig. 10(c) and (d). The electric field shows that a normal sheath, ion attracting and electron repelling, develops at the anode wall and there is no sign of sheath collapse as in Ref. 7. However, reverse sheaths can be found at the lateral dielectric walls. This avoids attracting ions and comply with the dielectric conditions at the walls since the curved magnetic topology effectively inhibits electron fluxes to the lateral dielectric walls. This is corroborated by the ion and electron current density streamlines plotted in Fig. 10(e) and (f). The scalar product of the electron current density and the electric field appears as an energy source in the electron energy equation. The power deposited by the electric field on the electron population per unit particle, in Fig. 10(g), peaks in the region immediately adjacent to the magnetic separatrix. This rises the electron temperature and leads to local maxima in T_e in this region, clearly visible in Fig. 10(h). From a microscopic perspective, only the most energetic electrons, with the largest Larmor radius, are capable of populating this region. The simulation results suggest that this unconventional feature of the local plasma response is a consequence of the combination of the magnetic topology and the dielectric condition at the lateral walls.

However, this result is dependent on the local features of the anomalous electron transport. A simulation doubling the anomalous diffusion in the thruster channel, thus leading to a higher higher I_d , does not show such abrupt changes in plasma properties at the location of the magnetic separatrix and the potential monotonically decreases towards the walls. This agrees with the fact that the higher the plasma collisionality, the higher electron mobility across magnetic field lines. The important changes in the plasma response imply that a proper characterization for anomalous transport is needed not only

along z but also along r .

VII. CONCLUSION

The 2D axial-radial PIC model of Ref. 7 (PICASO) has been improved to analyze more realistic HET discharges, considering cylindrical effects and a curved magnetic field topology. Electrons and singly charged ions are treated as two populations of macroparticles. Alternatively, neutrals are modeled as a background fluid. Ionization, excitation and elastic electron-neutral collisions are simulated with MCC algorithms. An empirical model for anomalous diffusion is included to account for electron transport induced by azimuthal instabilities. Acceleration techniques, such as a steady-state law for neutrals and an augmented vacuum permittivity, have been used to reduce the required computational cost.

The reference case simulates a virtual 5 kW class HET, which resembles PPS®5000. The magnetic topology features a large curvature near the anode and is almost radial near the exit. The time-evolution of currents to different domain boundaries shows convergence converge and steady-state solution is analyzed. Near the thruster exit, the results are similar to simulations with a purely radial magnetic field⁷. Near the anode the plasma features a complex 2D response. The approximate transition between the two regions is marked by a magnetic separatrix. Simulation results indicate that the curved magnetic field topology near the anode effectively reduces particle and energy fluxes to the lateral dielectric walls. The calculation of the wall interaction parameter $\tilde{\nu}_w$ used in 1Dz models of the discharge^{20,26} shows a strong dependence with the magnetic field curvature and justifies the value of $\tilde{\nu}_w = 0.17$ considered in previous works. Simulation results suggest that the normal Debye sheath may not be present for a grazing magnetic incidence. Near the anode, radial profiles show a plasma density concentrated in the channel center, away from the walls. The analysis of the radial momentum equation reveals that it consists of a balance between the pressure gradient, electric and magnetic force mainly. Near the thruster anode the strong curvature of the magnetic field induces a radially confining magnetic force which is compensated by the expanding pressure gradient term, while the electric force diminishes. This explains the observed trends in the radial profiles of macroscopic magnitudes. The axial electron momentum balance determines the azimuthal electron current, which is a result of $\mathbf{E} \times \mathbf{B}$ and diamagnetic drifts. The azimuthal electron momentum equation determines the axial electron current and shows an important contribution of FLR effects near the anode region.

The analysis of other simulation cases reveals that there is little difference in the results if a constant anomalous diffusion parameter is used instead of a step-out profile. However, the amount of anomalous diffusion inside the HET channel is crucial and affects significantly the

plasma response.

ACKNOWLEDGMENTS

This work has been supported by the R&D project HEEP (PID2022-140035OB-I00) funded by MCIN/AEI/10.13039/501100011033 and by “ERDF A way of making Europe”.

The authors thank E. Bello-Benítez for his contribution to the development of the original version of the code.

Appendix A: Effect of the augmentation factor of the vacuum permittivity

AM: Wall interaction, axial profiles and near anode maps

Appendix B: Effect of the number of simulated particles

AM: Wall interaction and axial profiles

Appendix C: Estimation of the numerical thermalization frequency

Estimation of the number of macroparticles per Debye volume. Taking the reference values in Table I: $n_e = 3 \cdot 10^{18} \text{ m}^{-3}$, $\lambda_{De} = 230 \mu\text{m}$ and $r_M = 65.5 \text{ mm}$.

$$N_D \simeq 2\pi r_M \lambda_{De}^2 n_e / w_p \simeq 100 \quad (\text{C1})$$

The characteristic relaxation time τ_R due to numerical thermalization can be estimated as

$$\omega_{pe} \tau_R = \frac{2\pi N_D}{0.98} \left[1 + \left(\frac{\Delta x}{\lambda_D} \right)^2 \right] \simeq 1126 \quad (\text{C2})$$

Thus, the numerical thermalization equivalent frequency is

$$\frac{1}{\tau_R} = \omega_{pe} / 1126 = 7.22 \cdot 10^6 \text{ s}^{-1} \quad (\text{C3})$$

while the anomalous collision frequency is

$$\nu_{ano} = \alpha_{ano} \omega_{ce} = 5.29 \cdot 10^7 \text{ s}^{-1} \quad (\text{C4})$$

An estimation for the inverse of the radial transit time gives

$$1/\tau_r = \bar{c}_e / L_r = 1.35 \cdot 10^8 \text{ s}^{-1} \quad (\text{C5})$$

The use of an increased vacuum permittivity leads to a numerical thermalization time that is longer than other phenomena affecting the electron velocity distribution function.

REFERENCES

- ¹A. Ortega, I. Mikellides, M. Sekerak, and B. Jorns, “Plasma simulations in 2-d (r-z) geometry for the assessment of pole erosion in a magnetically shielded Hall thruster,” *Journal of Applied Physics* **125** (2019).
- ²J. Perales-Díaz, A. Domínguez-Vázquez, P. Fajardo, E. Ahedo, F. Faraji, M. Reza, and T. Andreussi, “Hybrid plasma simulations of a magnetically shielded Hall thruster,” *Journal of Applied Physics* **131**, 103302 (2022).
- ³J. Bittencourt, *Fundamentals of plasma physics* (Springer, Berlin, Germany, 2004).
- ⁴E. Ahedo, “Using electron fluid models to analyze plasma thruster discharges,” *Journal of Electric Propulsion* **2**, 2 (2023).
- ⁵F. Taccogna and L. Garrigues, “Latest progress in Hall thrusters plasma modelling,” *Reviews of Modern Plasma Physics* **3**, 12 (2019).
- ⁶E. Bello-Benítez, A. Marín-Cebrián, and E. Ahedo, “Effect of injection conditions on the non-linear behavior of the ECDI and related turbulent transport,” (2024), pre-print available at <https://arxiv.org/pdf/2405.08761.pdf> [physics.plasm-ph].
- ⁷A. Marín-Cebrián, E. Bello-Benítez, A. Domínguez-Vázquez, and E. Ahedo, “Non-maxwellian electron effects on the macroscopic response of a hall thruster discharge from an axial–radial kinetic model,” *Plasma Sources Science and Technology* **33**, 025008 (2024).
- ⁸V. Kim, “Main physical features and processes determining the performance of stationary plasma thrusters,” *J. Propulsion Power* **14**, 736–743 (1998).
- ⁹R. Hofer and A. Gallimore, “The role of magnetic field topography in improving the performance of high-voltage Hall thrusters,” in *38th Joint Propulsion Conference*, AIAA 2002-4111 (Indianapolis, IN, 2002).
- ¹⁰J. Liu, H. Li, Y. Hu, X. Liu, Y. Ding, L. Wei, D. Yu, and X. Wang, “Particle-in-cell simulation of the effect of curved magnetic field on wall bombardment and erosion in a Hall thruster,” *Contributions to Plasma Physics* **59**, e201800001 (2019).
- ¹¹D. Ma, D. Zeng, L. Wang, Y. Ding, L. Wei, H. Li, and D. Yu, “Numerical simulation study on the influence of channel geometry on discharge characteristics of low-power magnetically shielded hall thrusters,” *Vacuum* **180**, 109547 (2020).
- ¹²A. Marín-Cebrián, A. Domínguez-Vázquez, P. Fajardo, and E. Ahedo, “Kinetic plasma dynamics in a radial model of a Hall thruster with a curved magnetic field,” *Plasma Sources Science and Technology* **31**, 115003 (2022).
- ¹³J. Miedzik, S. Barral, and D. Daničko, “Influence of oblique magnetic field on electron cross-field transport in a Hall effect thruster,” *Physics of Plasmas* **22**, 043511 (2015).
- ¹⁴A. Marín-Cebrián, E. Bello-Benítez, E. Ahedo, and A. Domínguez-Vázquez, “Kinetic electron effects in a Hall thruster discharge with a curved magnetic field topology,” in *38th International Electric Propulsion Conference*, IEPC-2024-387 (Electric Rocket Propulsion Society, Toulouse, France, June 23-28, 2024).
- ¹⁵C. Birdsall and A. Langdon, *Plasma Physics via Computer Simulation* (Institute of Physics Publishing, Bristol, 1991).
- ¹⁶A. Domínguez-Vázquez, F. Cichocki, M. Merino, P. Fajardo, and E. Ahedo, “Axisymmetric plasma plume characterization with 2D and 3D particle codes,” *Plasma Sources Science and Technology* **27**, 104009 (2018).
- ¹⁷Biagi, S.F., “Cross sections extracted from PROGRAM MAG-BOLTZ, version 7.1 june 2004,” (2004), [Online; accessed 5-July-2021].
- ¹⁸A. Domínguez-Vázquez, J. Zhou, A. Sevillano-González, P. Fajardo, and E. Ahedo, “Analysis of the electron downstream boundary conditions in a 2D hybrid code for Hall thrusters,” in *37th International Electric Propulsion Conference*,

- IEPC-2022-338 (Electric Rocket Propulsion Society, Boston, MA, USA, June 19-23, 2022).
- ¹⁹J. Szabo, N. Warner, M. Martinez-Sánchez, and O. Batishchev, “Full particle-in-cell simulation methodology for axisymmetric Hall effect thrusters,” *Journal of Propulsion and Power* **30**, 197–208 (2014).
- ²⁰E. Ahedo, J. Gallardo, and M. Martínez-Sánchez, “Effects of the radial-plasma wall interaction on the axial Hall thruster discharge,” *Physics of Plasmas* **10**, 3397–3409 (2003).
- ²¹A. Domínguez-Vázquez, F. Taccogna, and E. Ahedo, “Particle modeling of radial electron dynamics in a controlled discharge of a Hall thruster,” *Plasma Sources Science and Technology* **27**, 064006 (2018).
- ²²A. Marín-Cebrián, A. Domínguez-Vázquez, P. Fajardo, and E. Ahedo, “Macroscopic plasma analysis from 1D-radial kinetic results of a Hall thruster discharge,” *Plasma Sources Science and Technology* **30**, 115011 (2021).
- ²³I. Kaganovich, Y. Raitses, D. Sydorenko, and A. Smolyakov, “Kinetic effects in a Hall thruster discharge,” *Physics of Plasmas* **14**, 057104 (2007).
- ²⁴T. Charoy, T. Lafleur, A. Tavant, P. Chabert, and A. Bourdon, “A comparison between kinetic theory and particle-in-cell simulations of anomalous electron transport in ExB plasma discharges,” *Physics of Plasmas* **27**, 063510 (2020).
- ²⁵Y. Yamashita, R. Lau, and K. Hara, “Inertial and anisotropic pressure effects on cross-field electron transport in low-temperature magnetized plasmas,” *Journal of Physics D: Applied Physics* (2023).
- ²⁶E. Bello-Benitez and E. Ahedo, “Stationary axial model of the Hall thruster plasma discharge: electron azimuthal inertia and far plume effects,” *Plasma Sources Science and Technology* **32**, 115011 (2023).
- ²⁷D. Poli, E. Bello-Benítez, P. Fajardo, and E. Ahedo, “Time-dependent axial fluid model of the hall thruster discharge and its plume,” *Journal of Physics D: Applied Physics* (2023).
- ²⁸D. Poli, P. Fajardo, and E. Ahedo, “A non-neutral 1d fluid model of hall thruster discharges: full electron inertia and anode sheath reversal,” *Plasma Sources Science and Technology* **33**, 075014 (2024).
- ²⁹E. Ahedo and D. Escobar, “Two-region model for positive and negative plasma sheaths and its application to Hall thruster metallic anodes,” *Physics of Plasmas* **15**, 033504 (2008).

OTHER FIGURES AND TABLES

Reference simulation with $\alpha_t = \alpha_t(z, r) +$ Currents Discharge current (A) = 18.415175 A Discharge current (N) = 18.402437 A IiA = 0.293590 A IeA = 18.708765 A IiN = 15.930329 A IeNt = 101.021013 A IeNf = 103.493121 A IiW1 = 3.713867 A IeW1t = 7.753299 A IeW1f = 4.042187 A IiW2 = 1.903347 A IeW2t = 6.520557 A IeW2f = 4.617469 A + Power Discharge power (IdA*Vd) = 5524.552506 W Discharge power (IdN*Vd) = 5520.731009 W PiA = 1.689703 W PeA = 402.334747 W PiN = 3567.498291 W PeNt = 515.513672 W PeNf = 464.791412 W PiW1 = 490.656525 W PeW1t = 202.122681 W PeW1f = 1.614818 W PiW2 = 260.781158 W PeW2t = 230.879776 W PeW2f = 1.845160 W

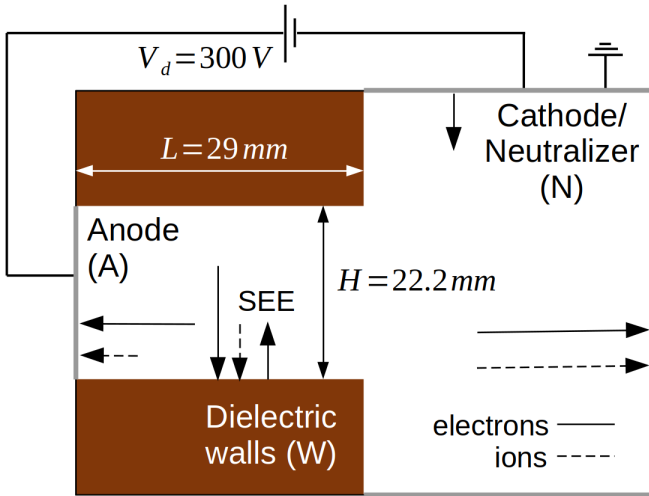


FIG. 1. Sketch of the simulation domain. Arrows indicate the expected direction of the electron (—) and ion (---) fluxes. The downstream plume boundary also acts as cathode/neutralizer, injecting electrons to satisfy continuity of the discharge current (between anode and cathode) at any instant.

Type	Description and symbol	Value and units
Physical system parameters	Channel inner radius, r_{W1}	54.5 mm
	Channel outer radius, r_{W2}	76.7 mm
	Channel length, L	29 mm
	Anode potential, ϕ_A	300 V
	Cathode potential, ϕ_N	0
	Mass flow, \dot{m}	17.59 mg/s
Surface interaction parameters	Wall cross-over energy, \mathcal{E}_c	50 eV
	SEE average emission energy, \mathcal{E}_{eWf}	0.4 eV
	Cathode average emission energy, \mathcal{E}_{eNf}	4.5 eV
Species settings	Initial plasma density, $n_{e0} = n_{i0}$	$4 \cdot 10^{17} \text{ m}^{-3}$
	Initial plasma temperature, $T_{e0} = T_{i0}$	1 eV
	Axial neutral velocity, u_{zn}	300 m/s
Characteristic plasma magnitudes	Debye length, λ_{De} (*)	230 μm
	Larmor radius, ρ_e	681 μm
	Inverse plasma frequency, ω_{pe}^{-1} (*)	123 ps
	Inverse gyrofrequency, ω_{ce}^{-1}	227 ps
Numerical parameters	Macroparticle weight, w_p	$6.59 \cdot 10^8$
	Grid spacing, $\Delta z = \Delta r$	200 μm
	Timestep, Δt	15 ps
	Simulated time, t_{sim}	60 μs
	Augmentation factor, f_D	12

TABLE I. Main input parameters for the 2Dzr PIC model. The characteristic plasma magnitudes have been calculated for $n_e = 3 \cdot 10^{18} \text{ m}^{-3}$, $T_e = 20 \text{ eV}$ and $B = 250 \text{ G}$. The Debye length and inverse plasma frequency, marked with an asterisk (*), are augmented by a factor f_D .

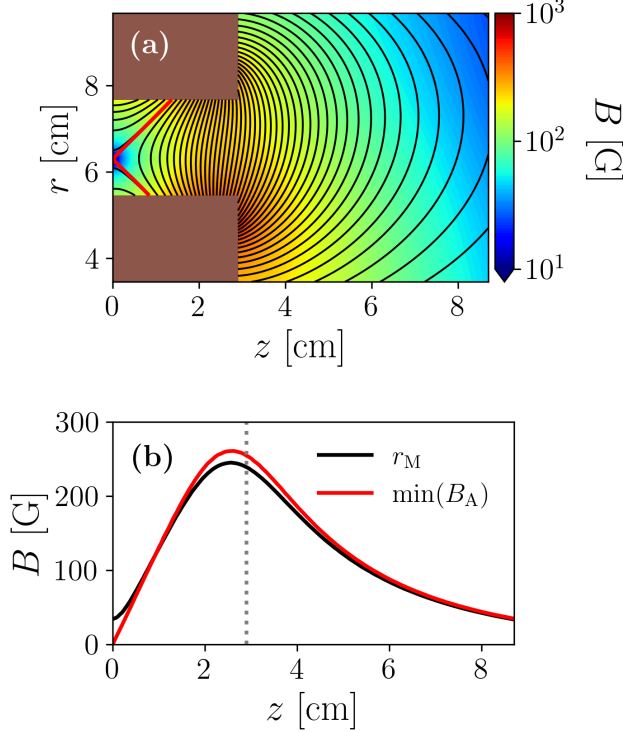


FIG. 2. Magnetic field topology: (a) shows a 2D plot of the imposed magnetic field, the black contours depict magnetic field lines, the red line represents the transition from magnetic field lines connecting the two lateral walls and those joining one of the lateral walls with the anode (b) plots axial profiles of the magnetic field magnitude at channel mean channel radius r_M and at the radial location of the minimum magnetic field at the anode $\min(B_A) \approx 0.2$ G at $r = 62.9$ mm. At $z \approx 8.46$ mm, the magnetic separatrix intersects the inner wall. At $z \approx 13.65$ mm, the magnetic separatrix intersects the outer wall. **AM: Subíndice para la posición del campo magnético mínimo.**

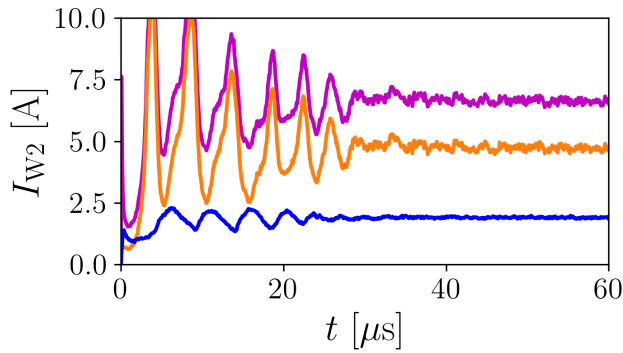


FIG. 3. Time evolution of the electron and ion currents to the outer wall: ions reaching the wall, $|I_{iW2}|$ (blue); electrons reaching the wall, $|I_{eW2r}|$ (purple); and electrons emitted from the wall (SEE), $|I_{eW2f}|$ (orange).

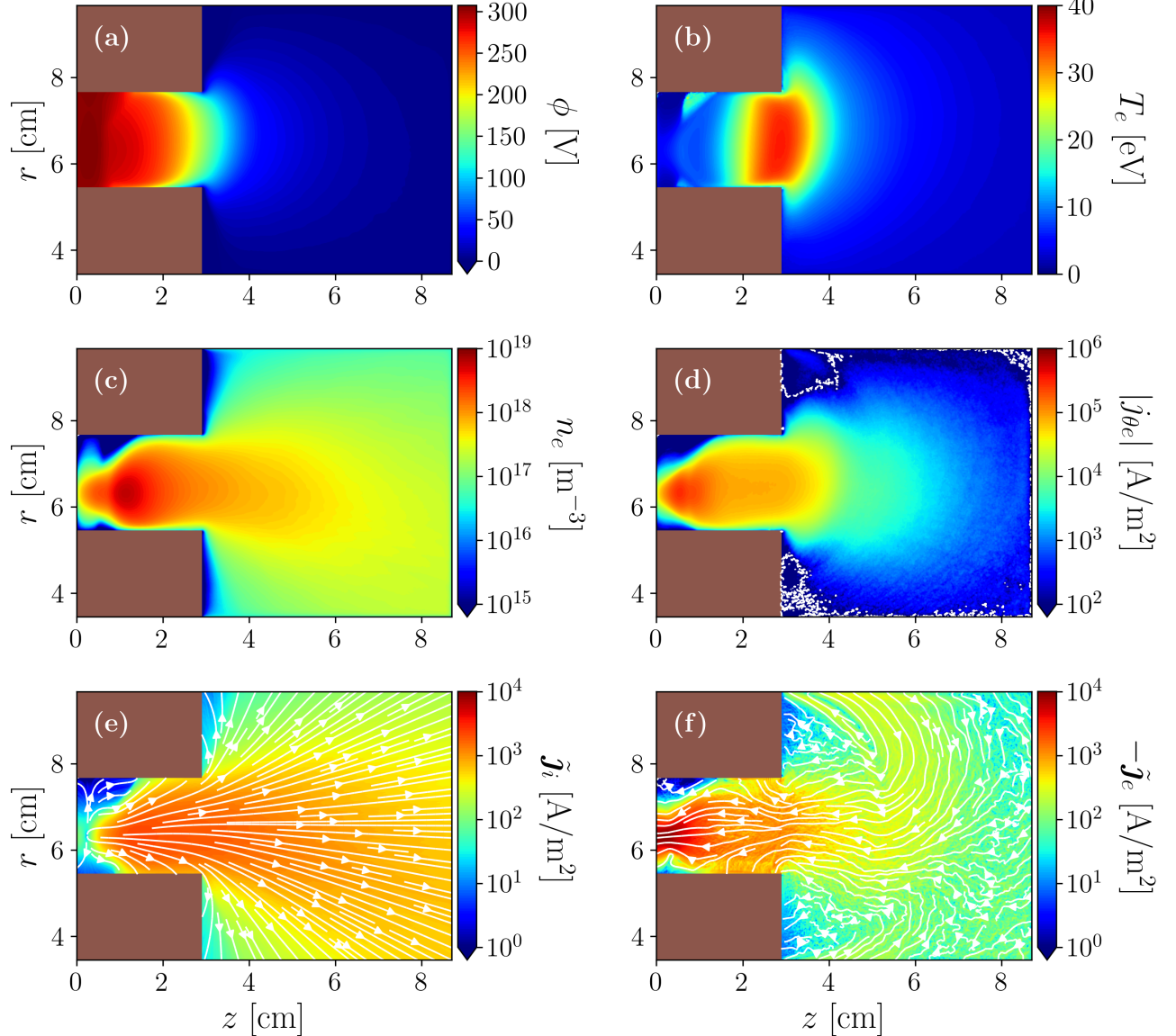


FIG. 4. Maps of the main macroscopic variables characterizing the reference case simulation at steady-state: (a) electric potential, (b) electron temperature, (c) electron density, (d) azimuthal electron current, (e) and (f) longitudinal ion and electron current densities respectively. The white contour lines indicate a change of sign in $j_{\theta e}$. **AM: Quitar las corrientes de iones y electrones? Quitar la parte de $u_{\theta e} < 0$**

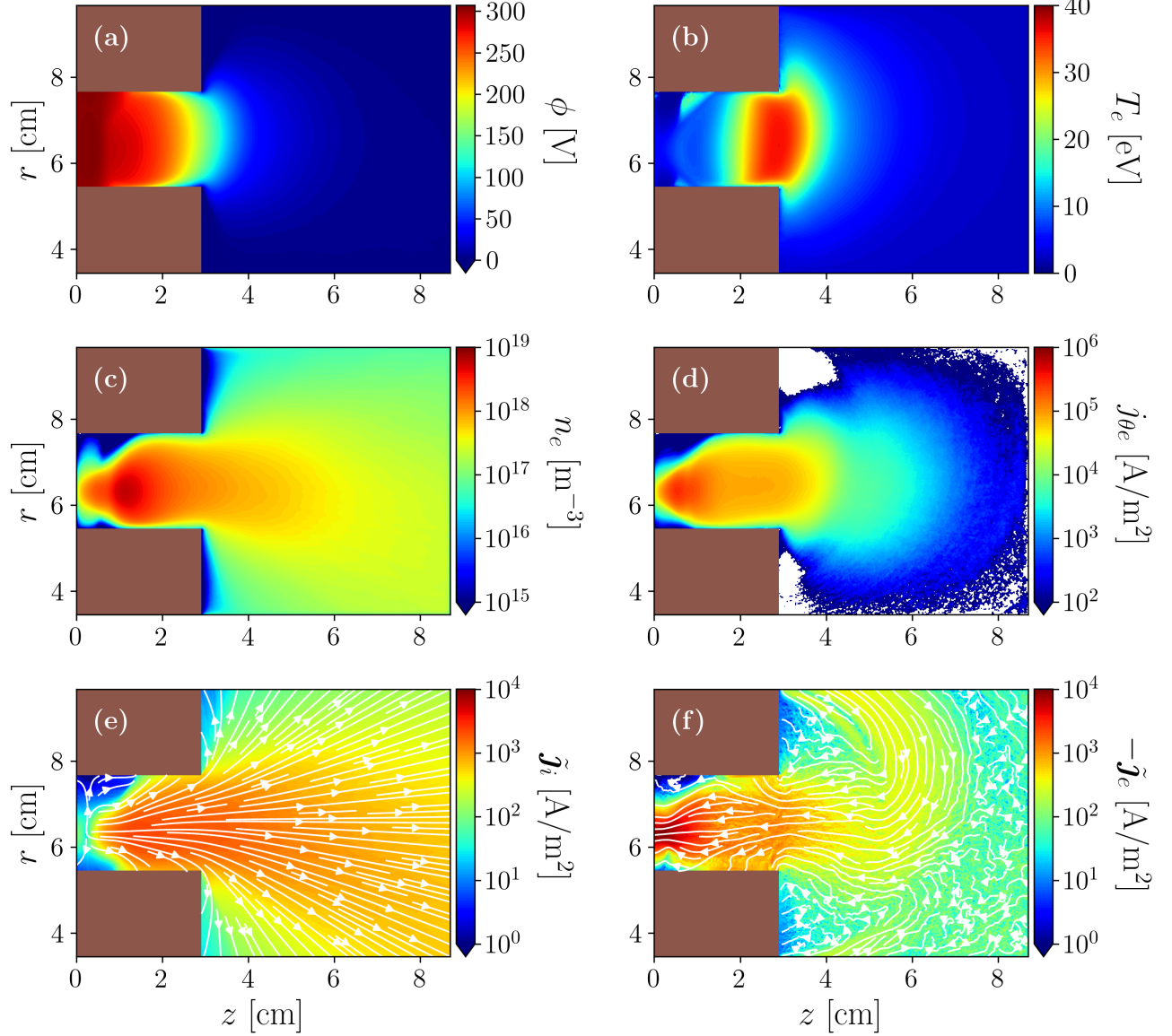


FIG. 5. Maps of the main macroscopic variables characterizing the reference case simulation at steady-state: (a) electric potential, (b) electron temperature, (c) electron density, (d) azimuthal electron current, (e) and (f) longitudinal ion and electron current densities respectively.

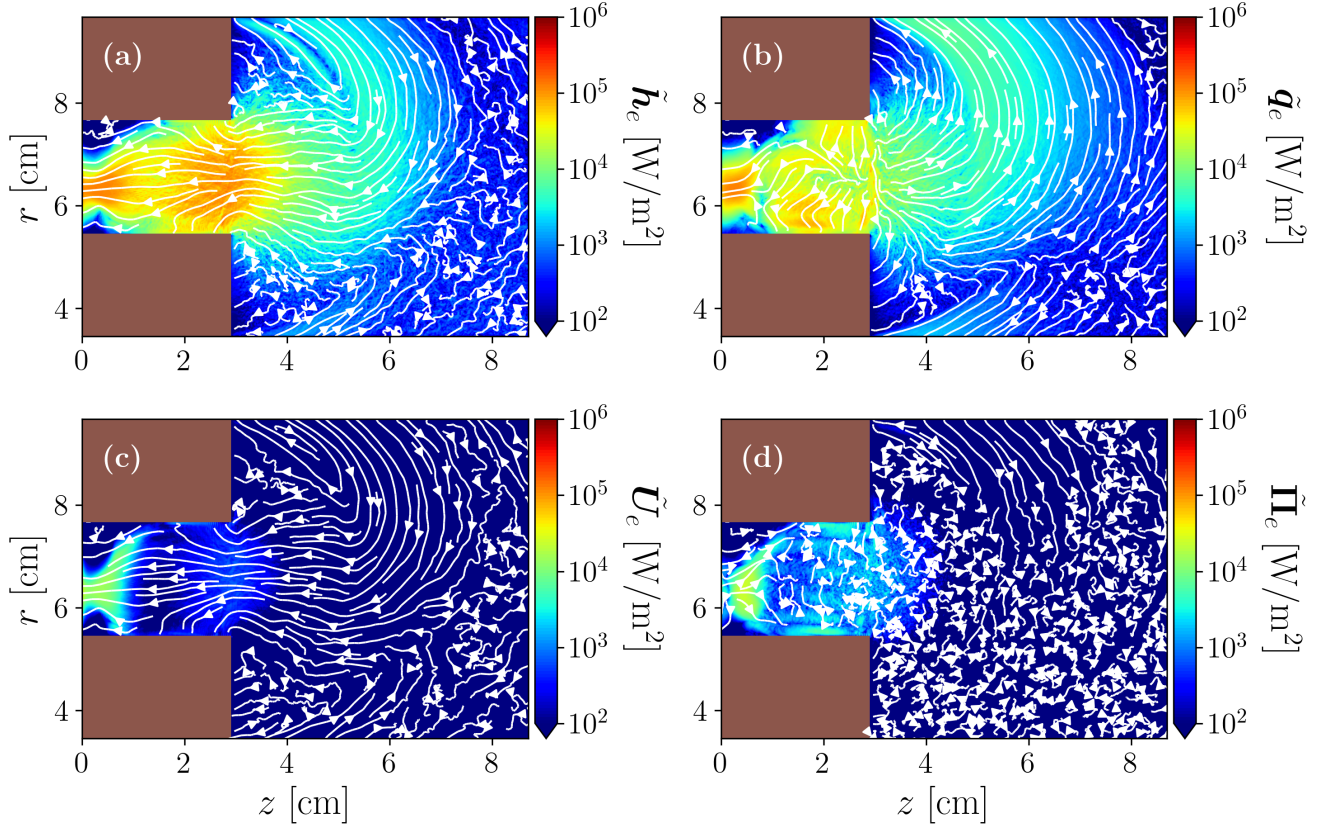


FIG. 6. Longitudinal electron energy flux vector contributions: (a) enthalpy flux, (b) heat flux, (c) fluid flow energy flux, and (d) gyrostress contribution.

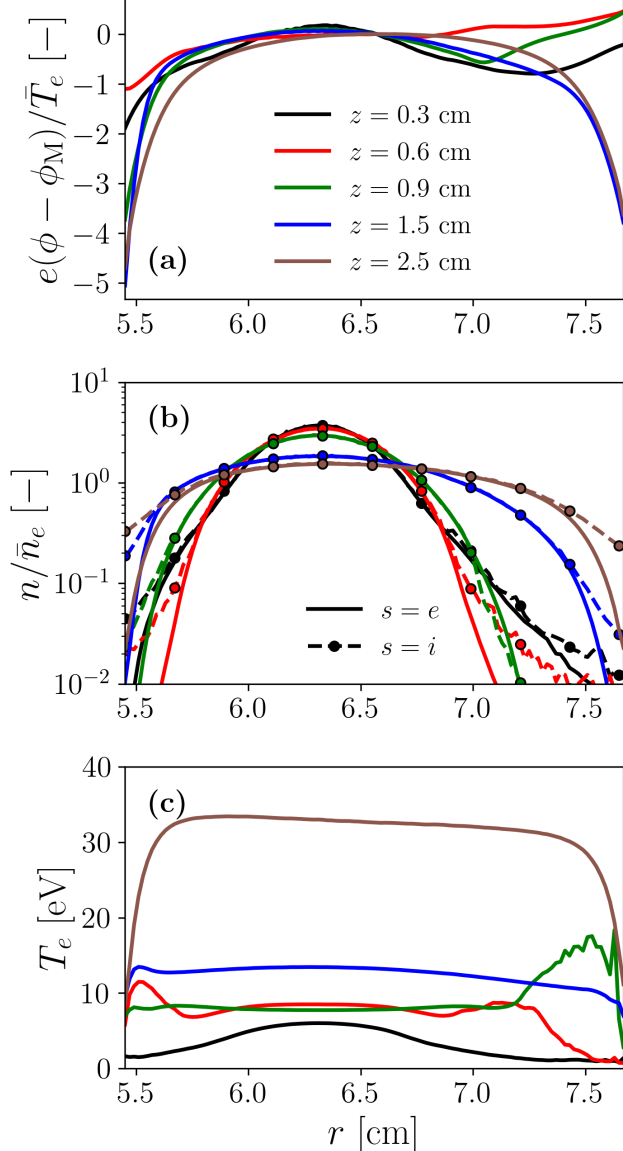


FIG. 7. Radial profiles of steady-state macroscopic variables for the reference case simulation at different axial locations: (a) non-dimensional electric potential, (b) non-dimensional ion and electron densities, (c) electron scalar temperature.

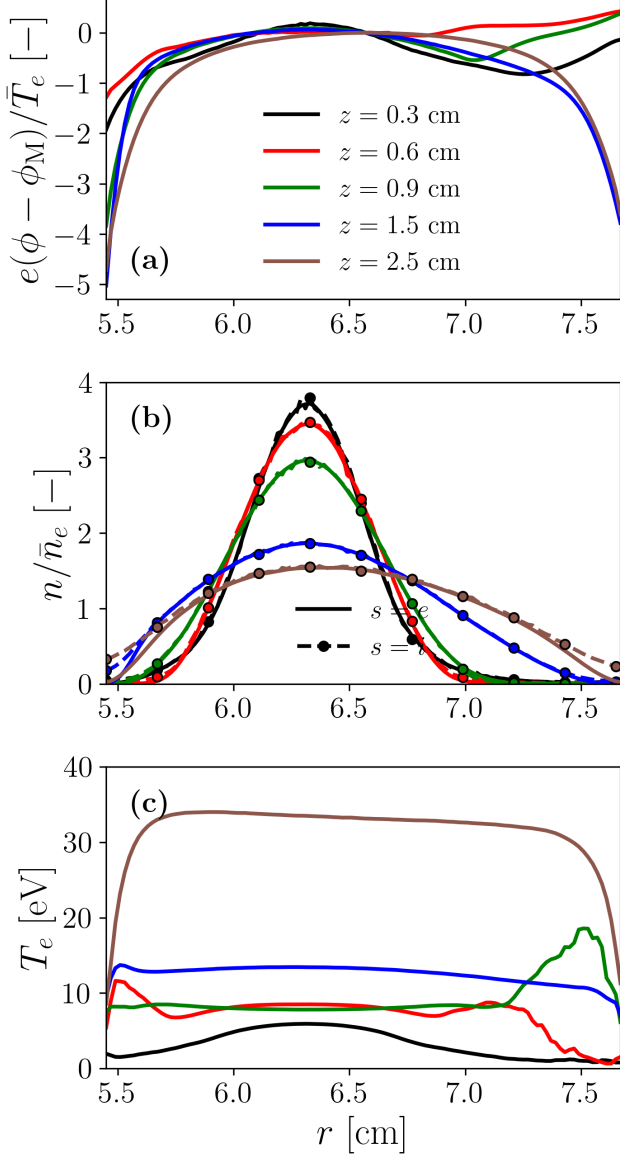


FIG. 8. Radial profiles of steady-state macroscopic variables for the reference case simulation at different axial locations: (a) non-dimensional electric potential, (b) non-dimensional ion and electron densities, (c) electron scalar temperature.

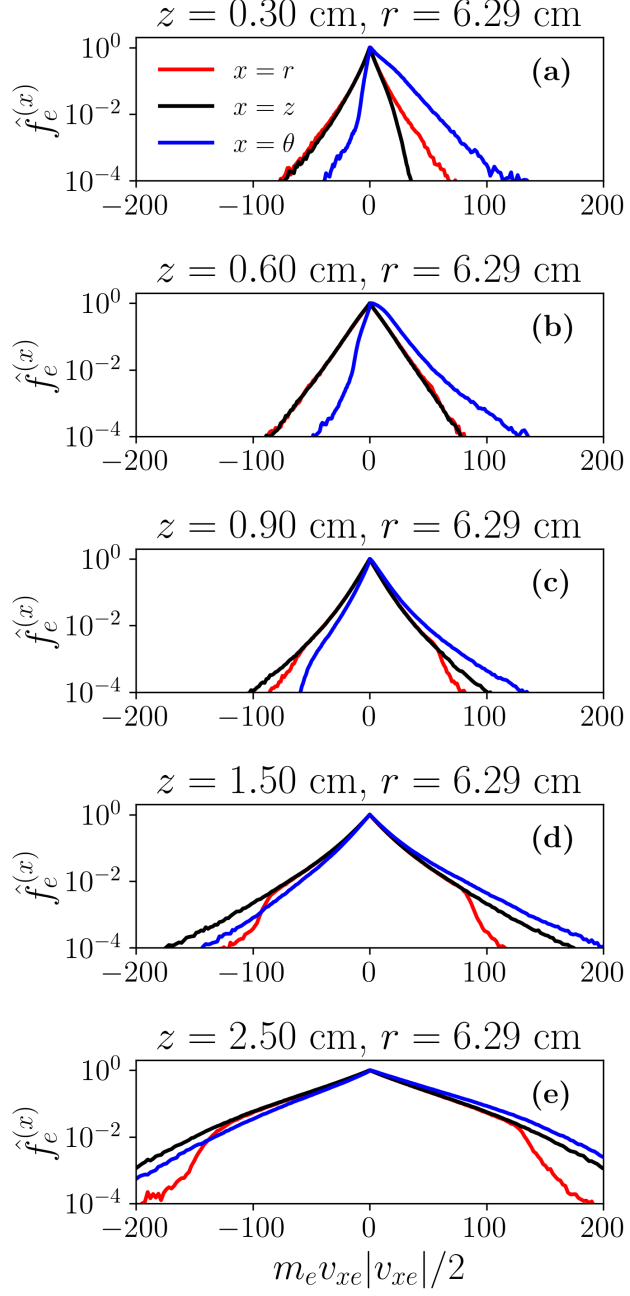


FIG. 9. Electron VDFs at different locations inside the HET channel.

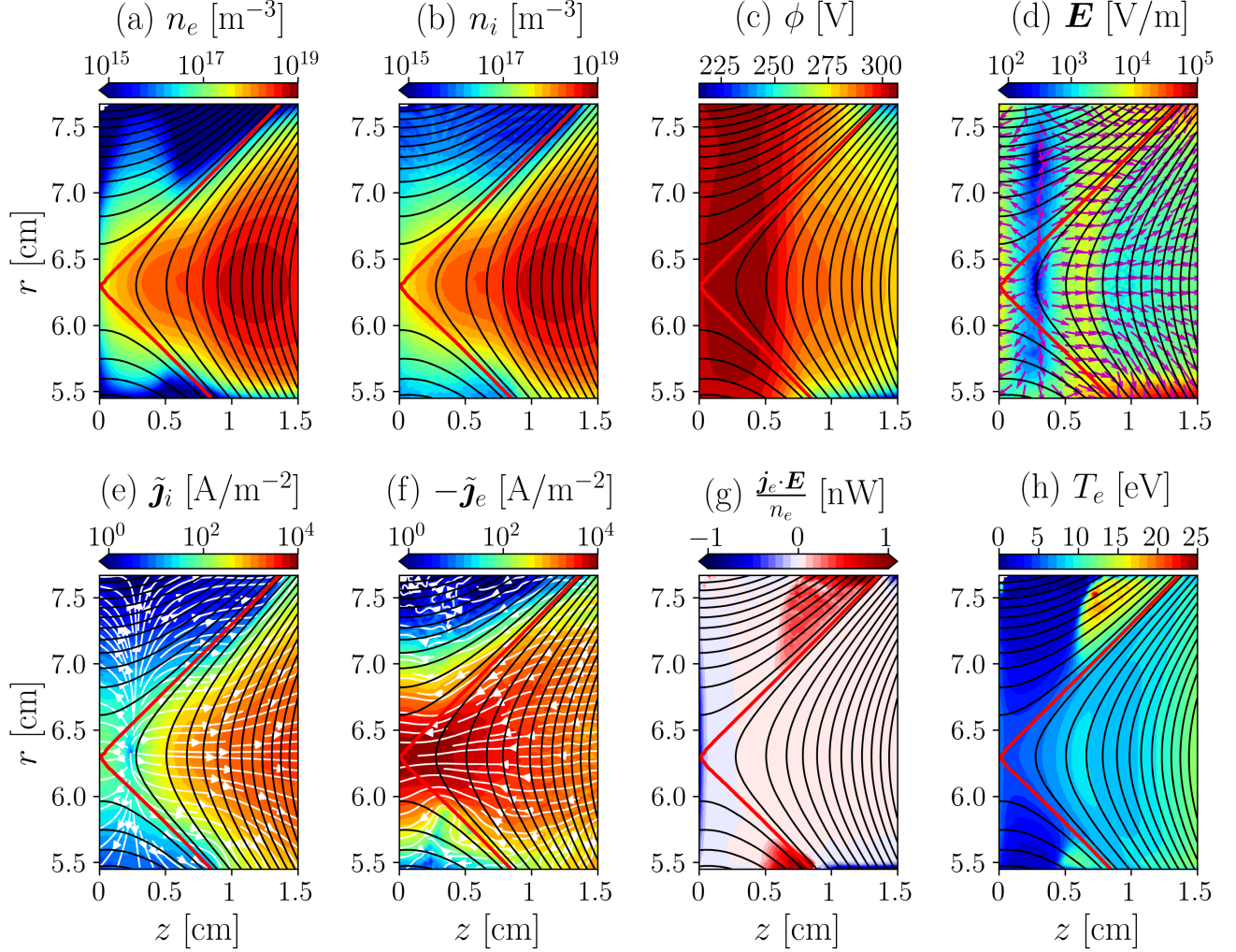


FIG. 10. Macroscopic plasma variables near the anode: (a) electron density, n_e ; (b) ion density, n_i ; (c) electric potential, ϕ ; (d) electric field, \mathbf{E} ; (e) longitudinal ion current density, $\tilde{\mathbf{j}}_i$; (f) longitudinal electron current density, $\tilde{\mathbf{j}}_e$; (g) power of the electric field on the electron population per unit particle, $\mathbf{j}_e \cdot \mathbf{E}/n_e$; (h) scalar electron temperature, T_e . Black contours represent magnetic field lines and the magnetic separatrix is plotted in red. **AM: cambiar la notación de (g)** $-e\mathbf{u}_e \cdot \mathbf{E}$

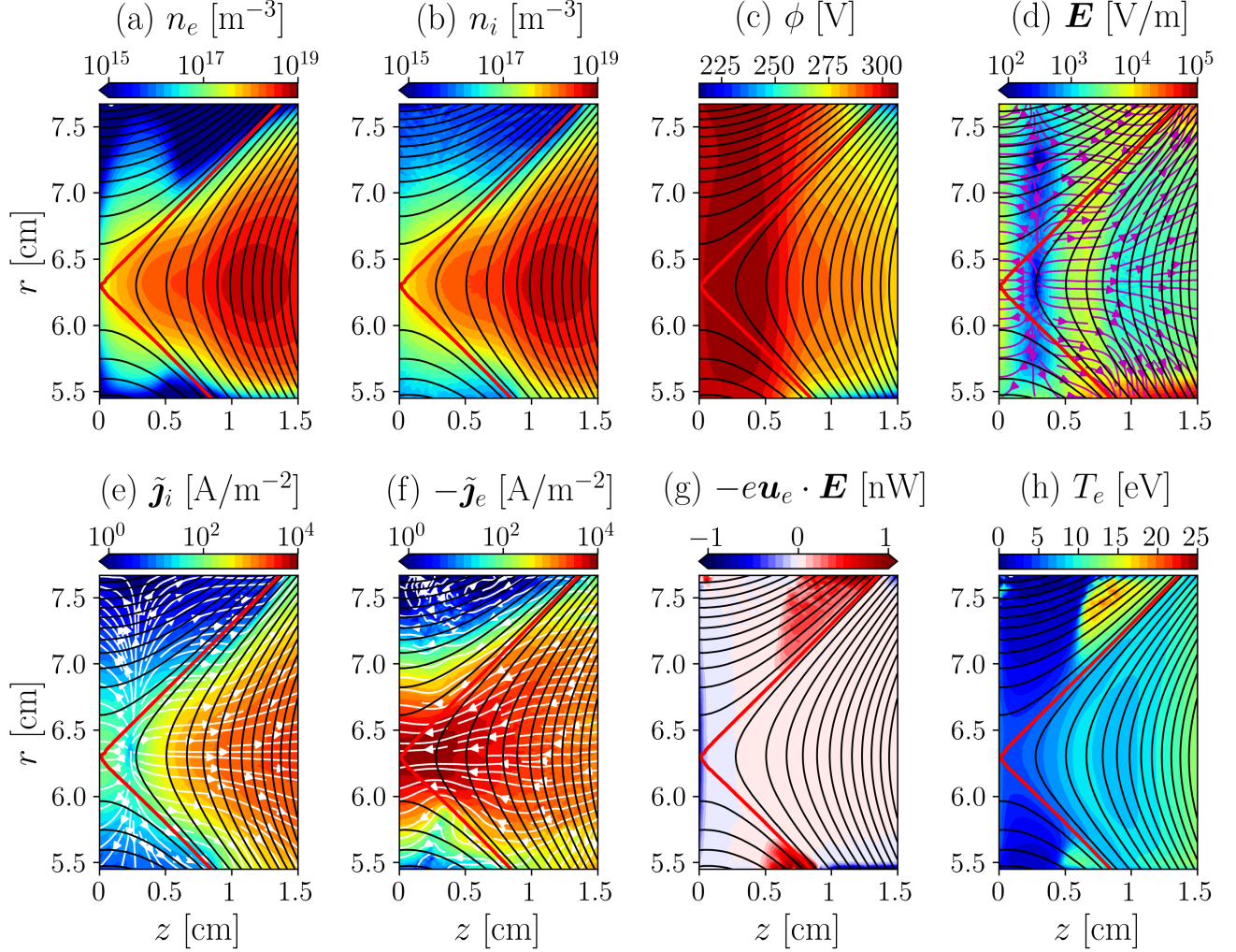


FIG. 11. Macroscopic plasma variables near the anode: (a) electron density, n_e ; (b) ion density, n_i ; (c) electric potential, ϕ ; (d) electric field, \mathbf{E} ; (e) longitudinal ion current density, $\tilde{\mathbf{j}}_i$; (f) longitudinal electron current density, $\tilde{\mathbf{j}}_e$; (g) power of the electric field on the electron population per unit particle, $-e\mathbf{u}_e \cdot \mathbf{E}$; (h) scalar electron temperature, T_e . Black contours represent magnetic field lines and the magnetic separatrix is plotted in red.

Description and symbol	Value and units
Discharge current, I_d	18.42 A
Ion current to the anode, $ I_{iA} $	0.29 A
Electron current to the anode, $ I_{eA} $	18.71 A
Ion current to the inner wall, $ I_{iW_1} $	3.71 A
Electron current to the inner wall, $ I_{eW_1t} $	7.75 A
SEE current from the inner wall, $ I_{eW_1f} $	4.04 A
Ion current to the outer wall, $ I_{iW_2} $	1.90 A
Electron current to the outer wall, $ I_{eW_2t} $	6.52 A
SEE current from the outer wall, $ I_{eW_2f} $	4.62 A
Discharge power, $I_d V_d$	5525 W
Ion power to the anode, P_{iA}	2 W
Electron power to the anode, P_{eA}	402 W
Ion power to the inner wall, P_{iW_1}	491 W
Electron power to the inner wall, P_{eW_1t}	202 W
SEE power from the inner wall, P_{eW_1f}	2 W
Ion power to the outer wall, P_{iW_2}	261 W
Electron power to the outer wall, P_{eW_2t}	231 W
SEE power from the outer wall, P_{eW_2f}	2 W

TABLE II. Current and power deposited at different surfaces.

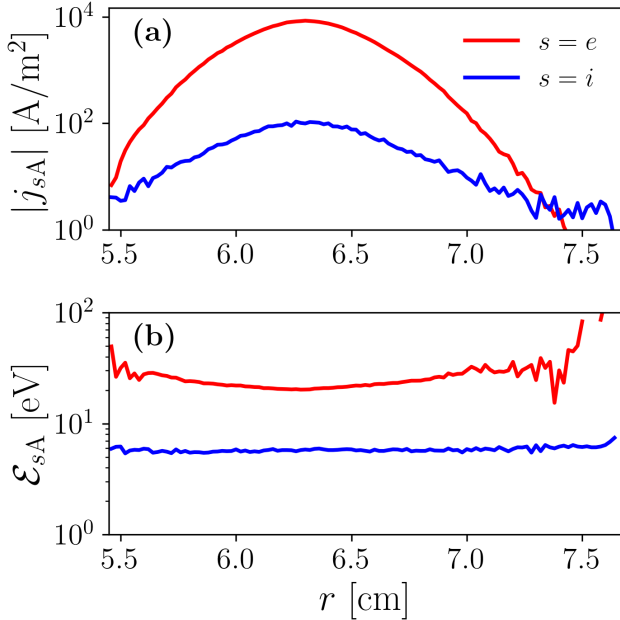


FIG. 12. Wall interaction magnitudes at the anode: (a) current densities, and (b) average impact energies for electrons and ions.

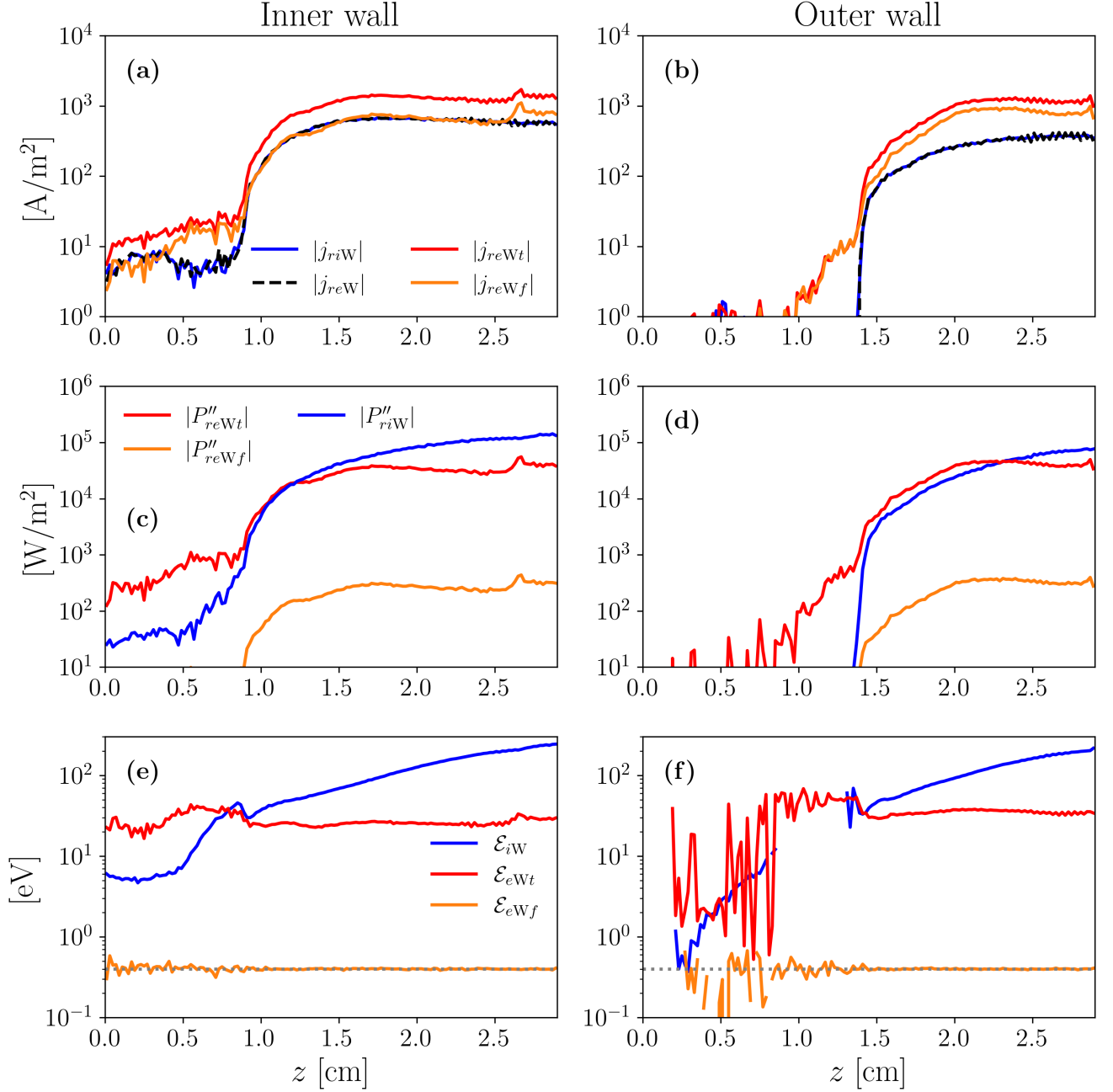


FIG. 13. Wall interaction magnitudes at the inner wall, left column plots, and outer wall, right column plots: (a), (b) ion current density to the wall j_{riW} , electron current density to the wall j_{reWt} , and electron current density from the wall (SEE) j_{reWf} ; (c), (d) ion energy flux to the wall P''_{riW} , electron energy flux to the wall P''_{reWt} , and electron (SEE) energy flux from the wall P''_{reWf} ; and (e), (f) ion energy to the wall \mathcal{E}_{iW} , electron energy to the wall \mathcal{E}_{eWt} , and electron (SEE) energy from the wall \mathcal{E}_{eWf} . **AM: Eliminar las energías de impacto em pared?**

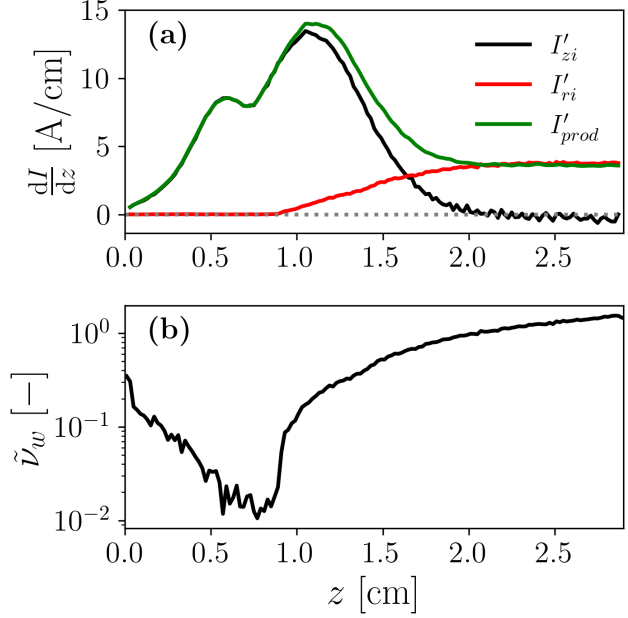


FIG. 14. (a) Current continuity balance showing the contributions of the different terms in Eq. (7) for the ion population. The notation ' $\equiv d/dz$ ' is used in the legend. (b) Non-dimensional wall collisionality parameter defined as in Ref. 26 [Eq. (9)].

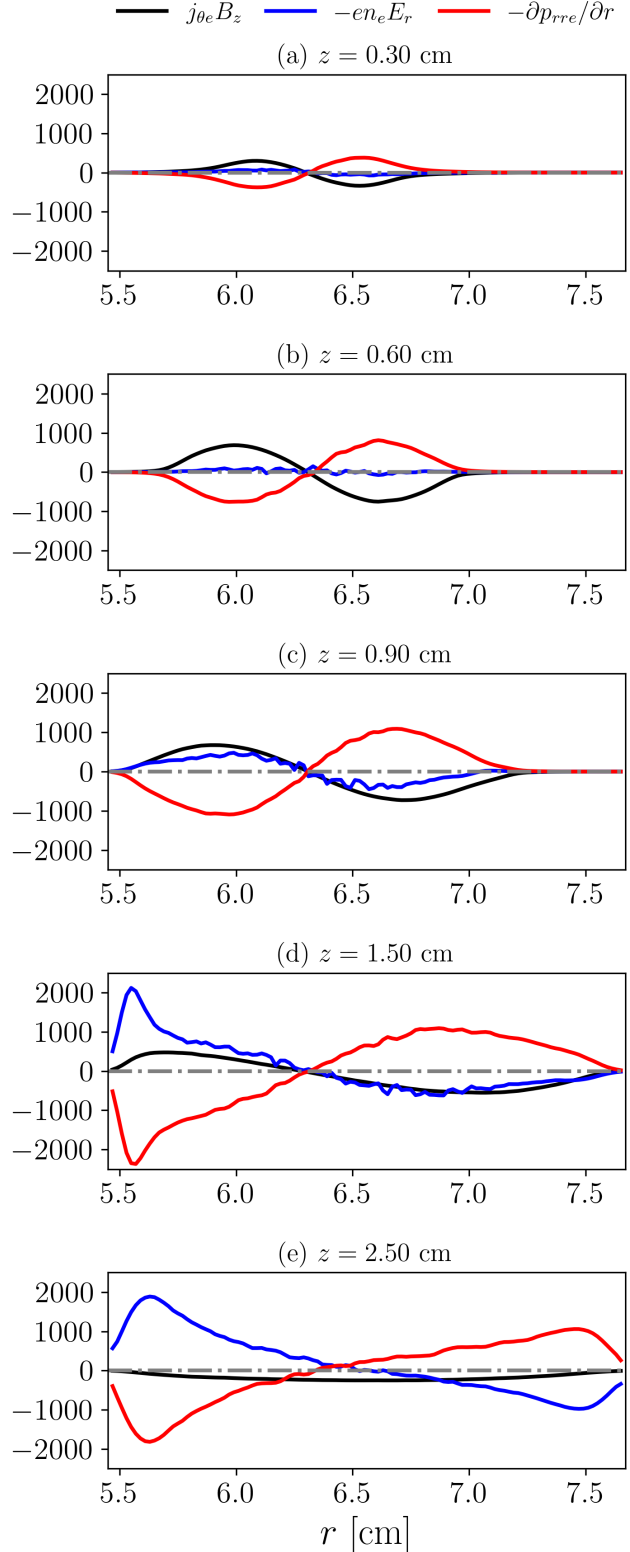


FIG. 15. Main contributions to the radial momentum equation [Eq. (4)] at five different axial sections in N/m^3 .

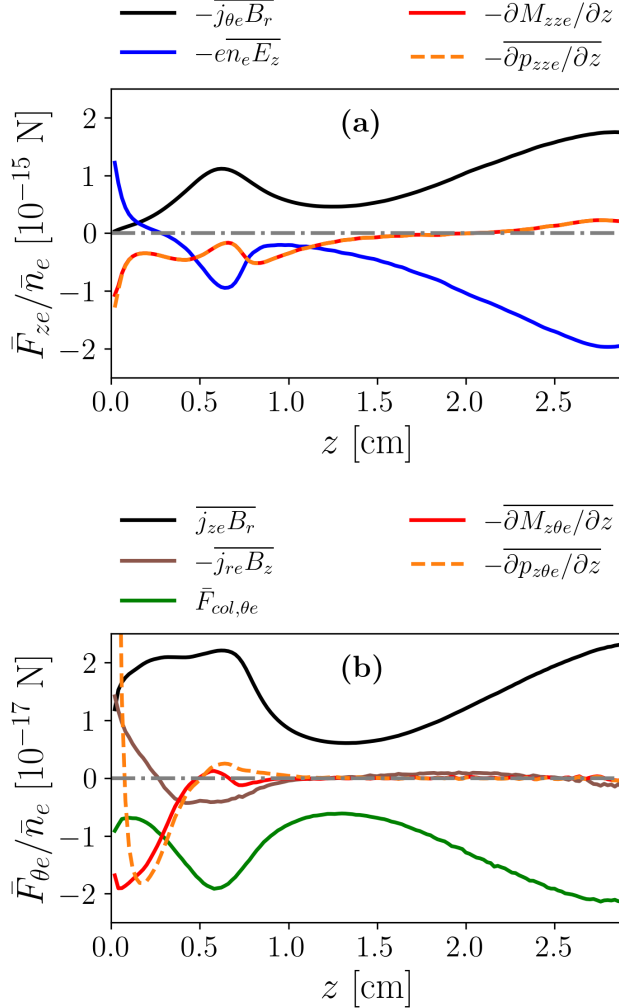


FIG. 16. Radially averaged electron momentum balance: (a) contributions to the axial electron momentum balance, (—) $-\overline{j_{\theta e} B_r}$, ...

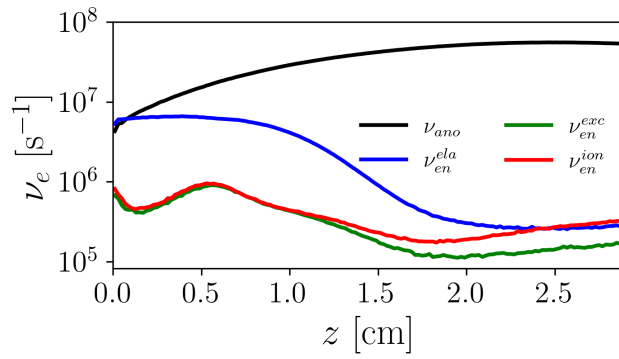


FIG. 17. Radially averaged value of the collision frequencies. $\overline{n_e \nu_e}/\bar{n}_e$

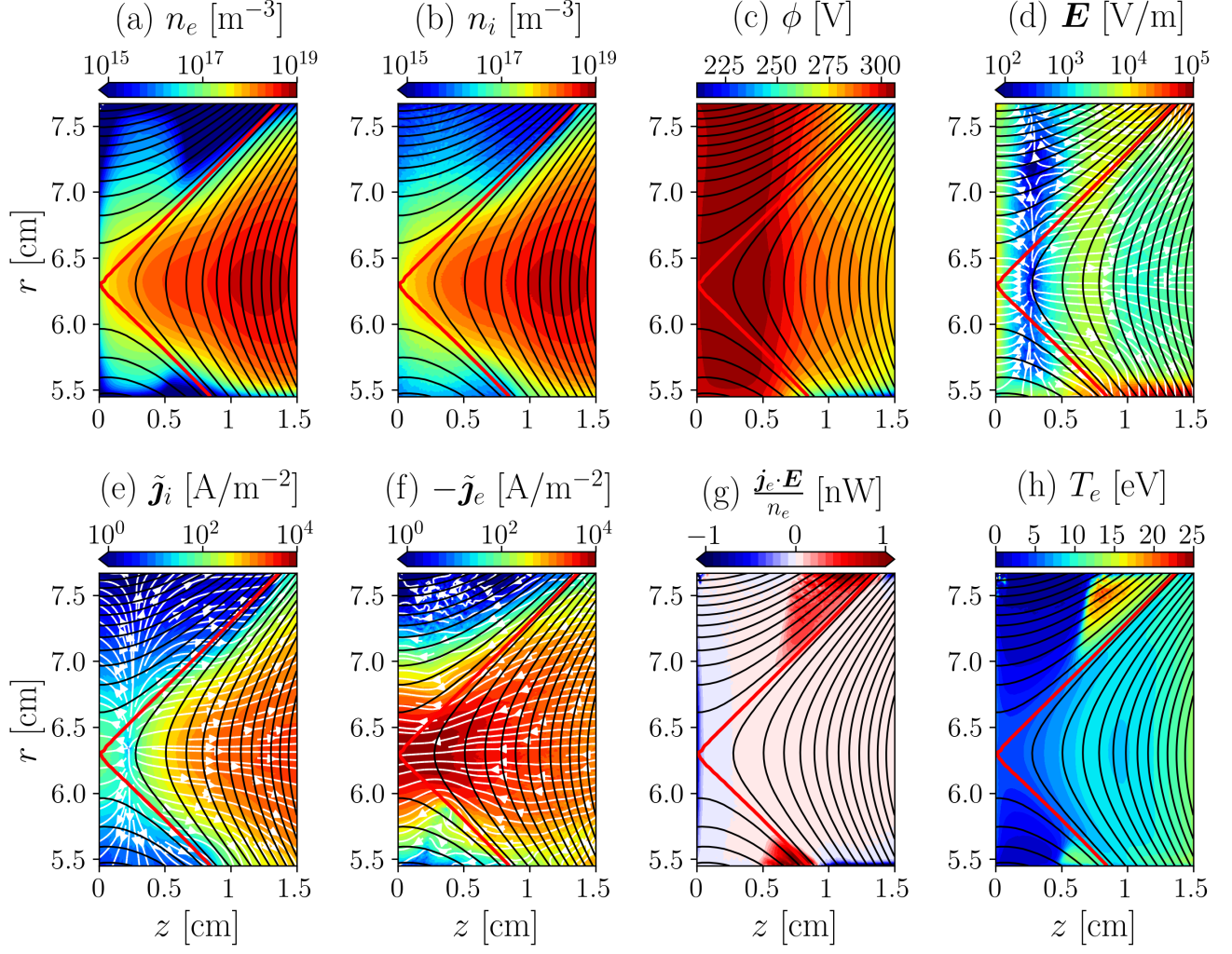


FIG. 18. Macroscopic plasma variables near the anode for the simulation with $f_D = 8$. [AM: Decidir qué figuras mantenemos para el apéndice](#)

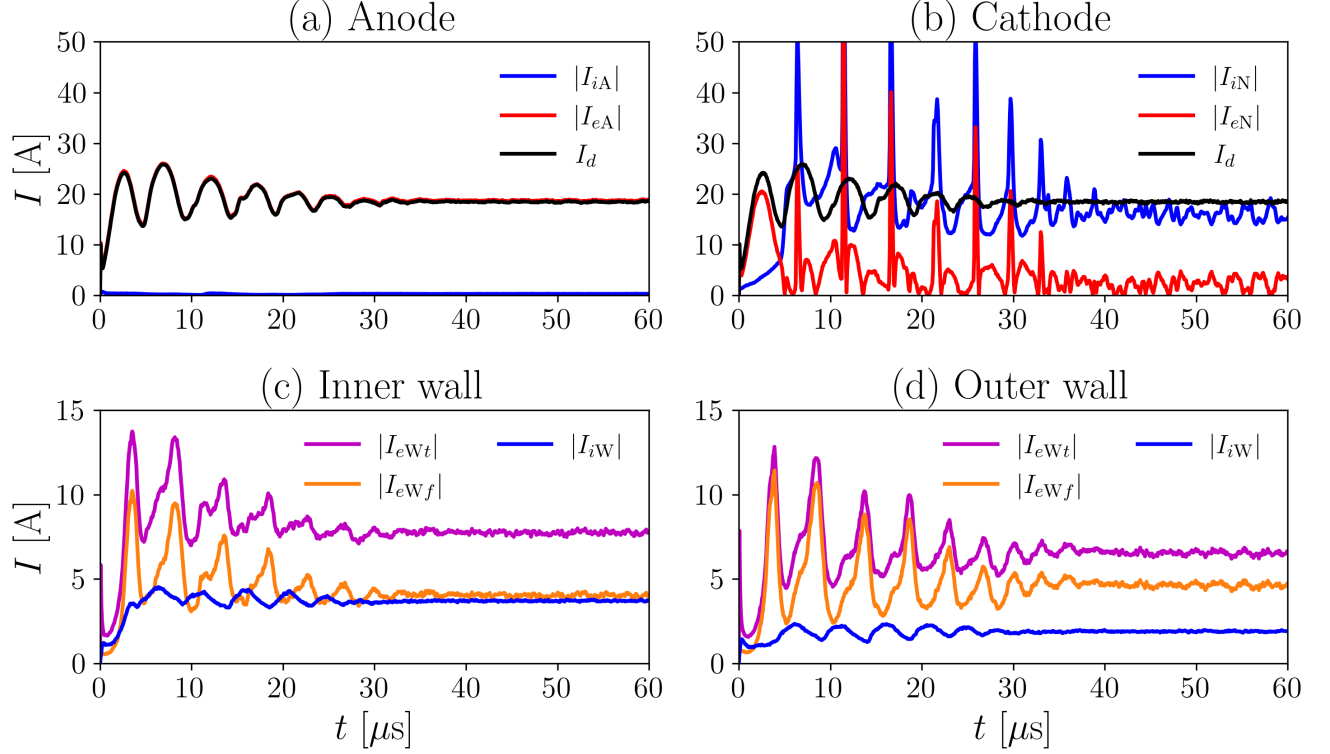


FIG. 19. Time evolution of electron and ion currents to important boundary surfaces: (a) anode, (b) virtual cathode, (c) inner dielectric wall, and (d) outer dielectric wall of the simulated thruster. EA: la mitad de la figura a esta usada por la leyenda y no es posible saber cuánto vale la corriente de iones AM: Dejar solo outer wall

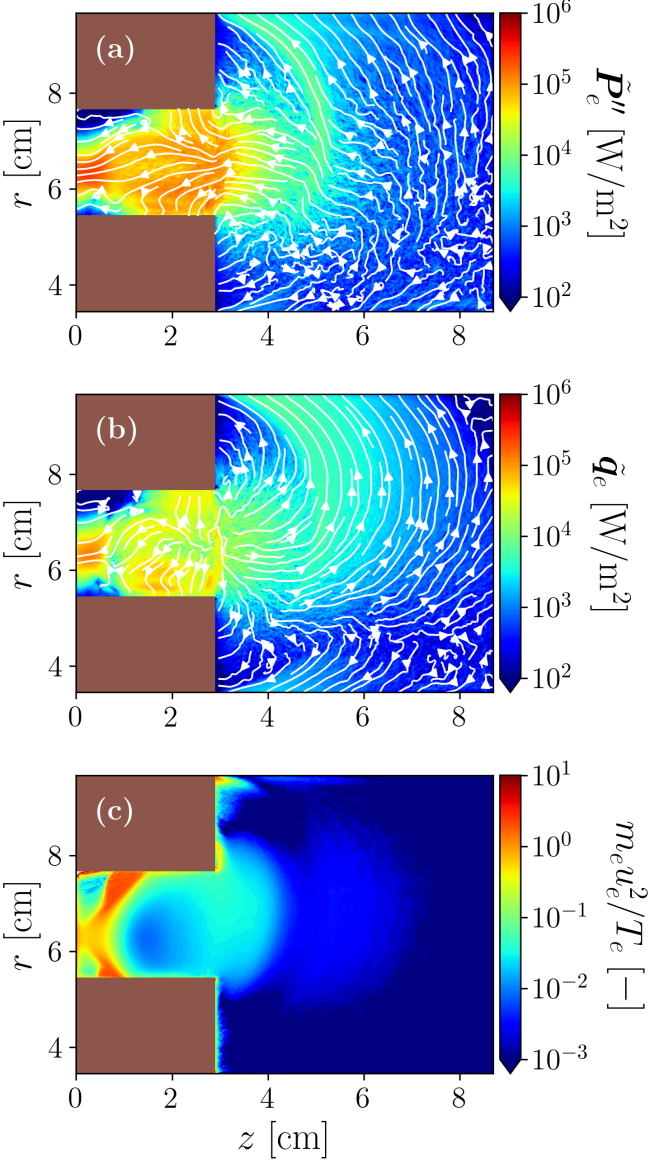


FIG. 20. Radial profiles of electron energy related variables:
 (a) electron energy flux vector, (b) electron heat flux vector,
 (c) ratio between electron inertia and temperature. **AM:**
[Mapas 2D de las distintas componentes de \$P_e''\$](#)

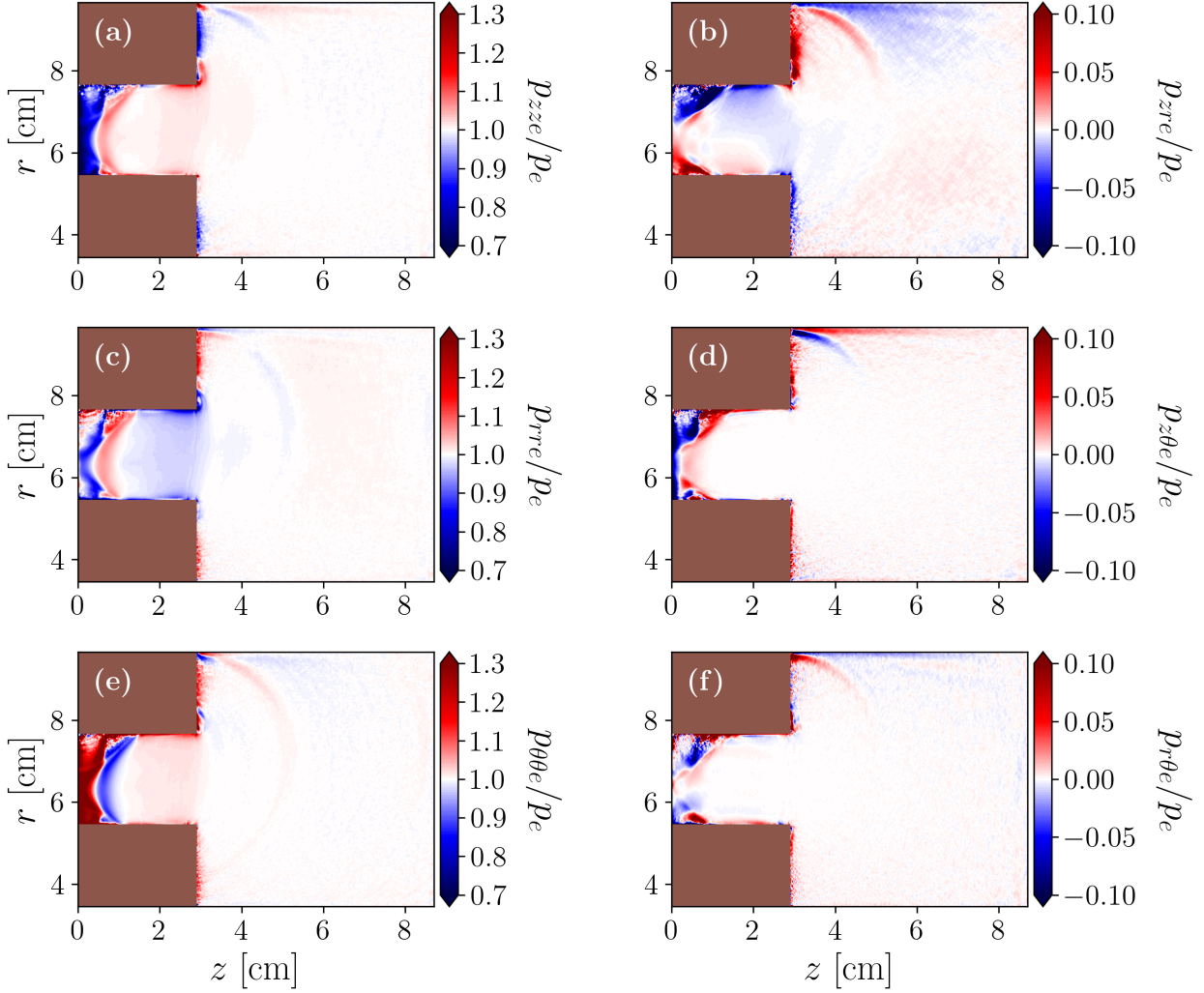


FIG. 21. Pressure tensor components normalized with respect to the scalar pressure $p_e = (p_{zze} + p_{rre} + p_{\theta\theta e})/3$. **AM: guitar y hacer el comentario con las VDFs**

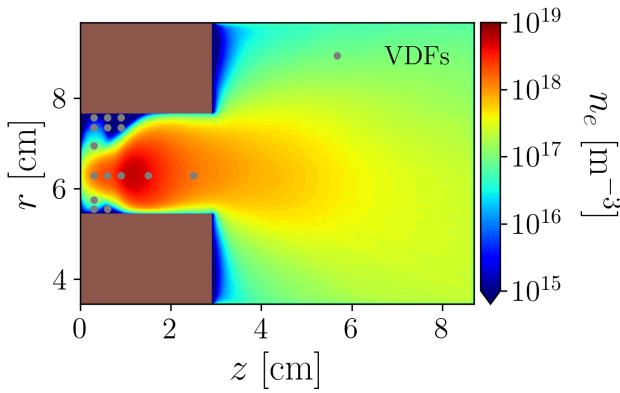


FIG. 22. Locations where the electron and ion VDFs are computed.

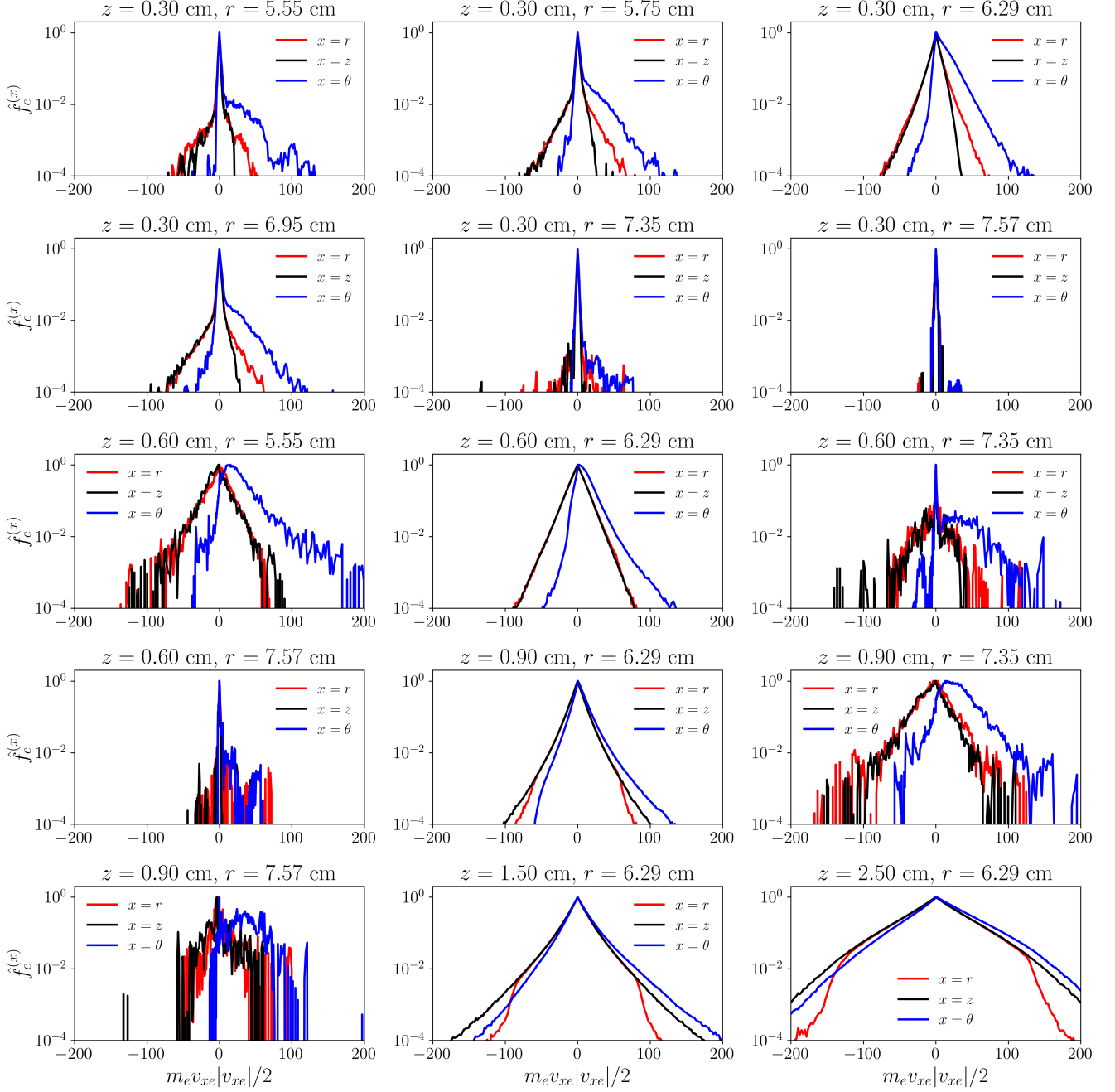


FIG. 23. Electron VDFs at different locations **AM: VDFs en $r = 6.29$**

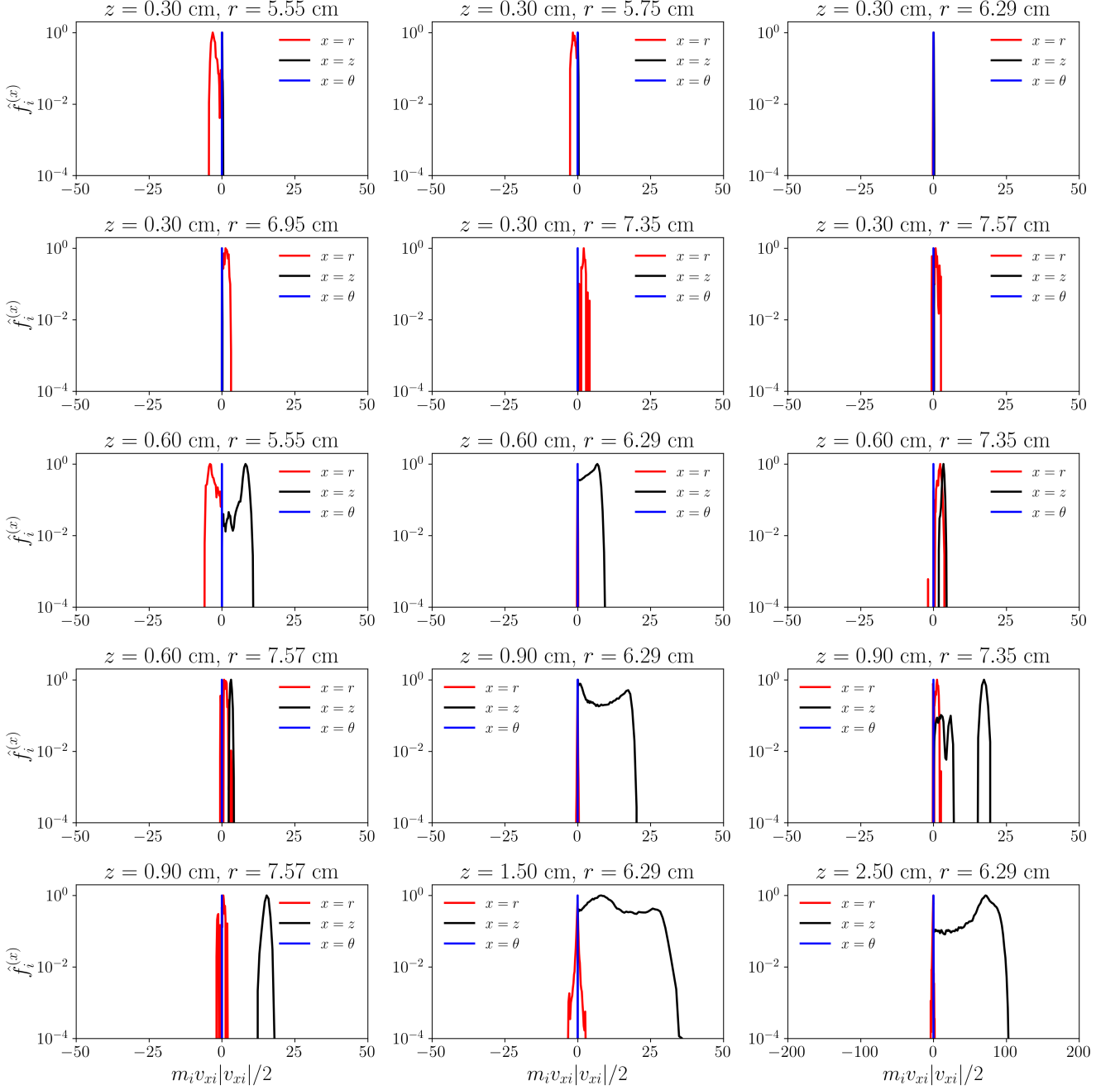


FIG. 24. Ion VDFs at different locations **AM: anisotropia: nos quedamos con la 31, 32, 52**

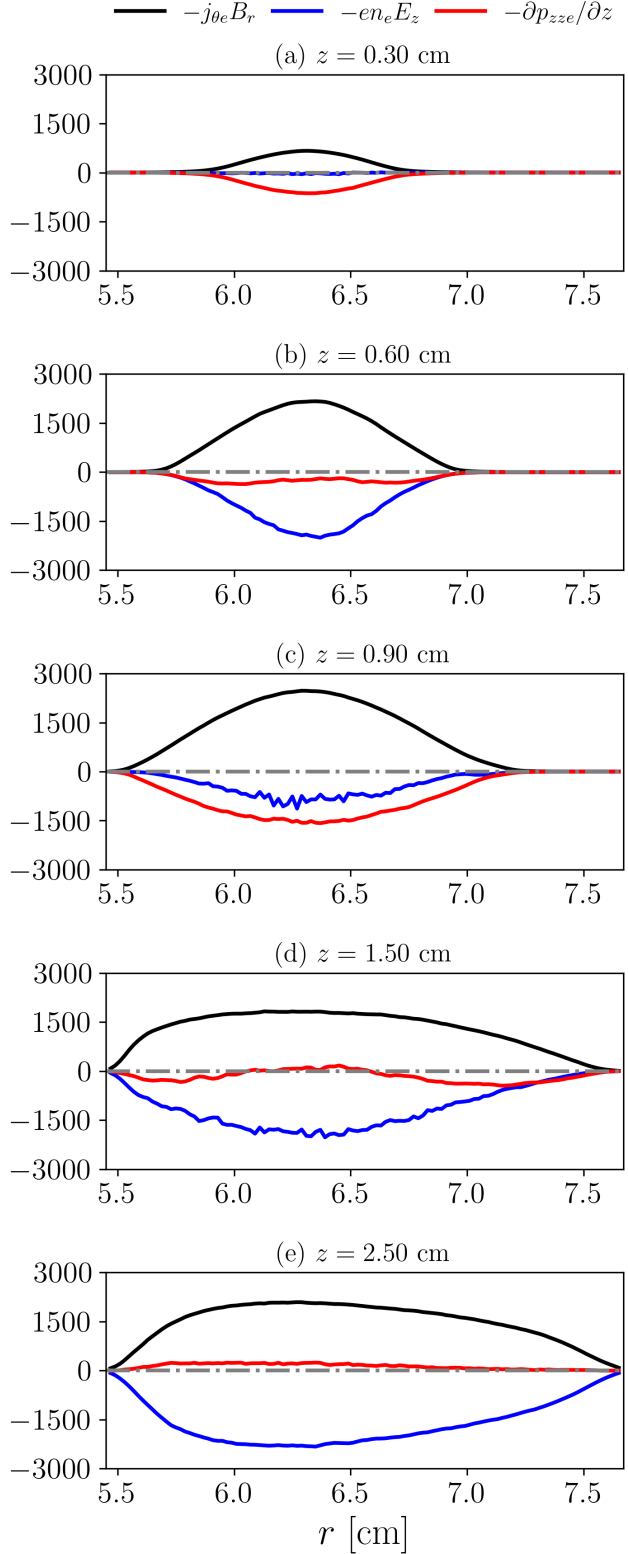


FIG. 25. Main contributions to the axial momentum equation [Eq. (5)] at five different axial sections in N/m^3 . **AM:** Eliminar

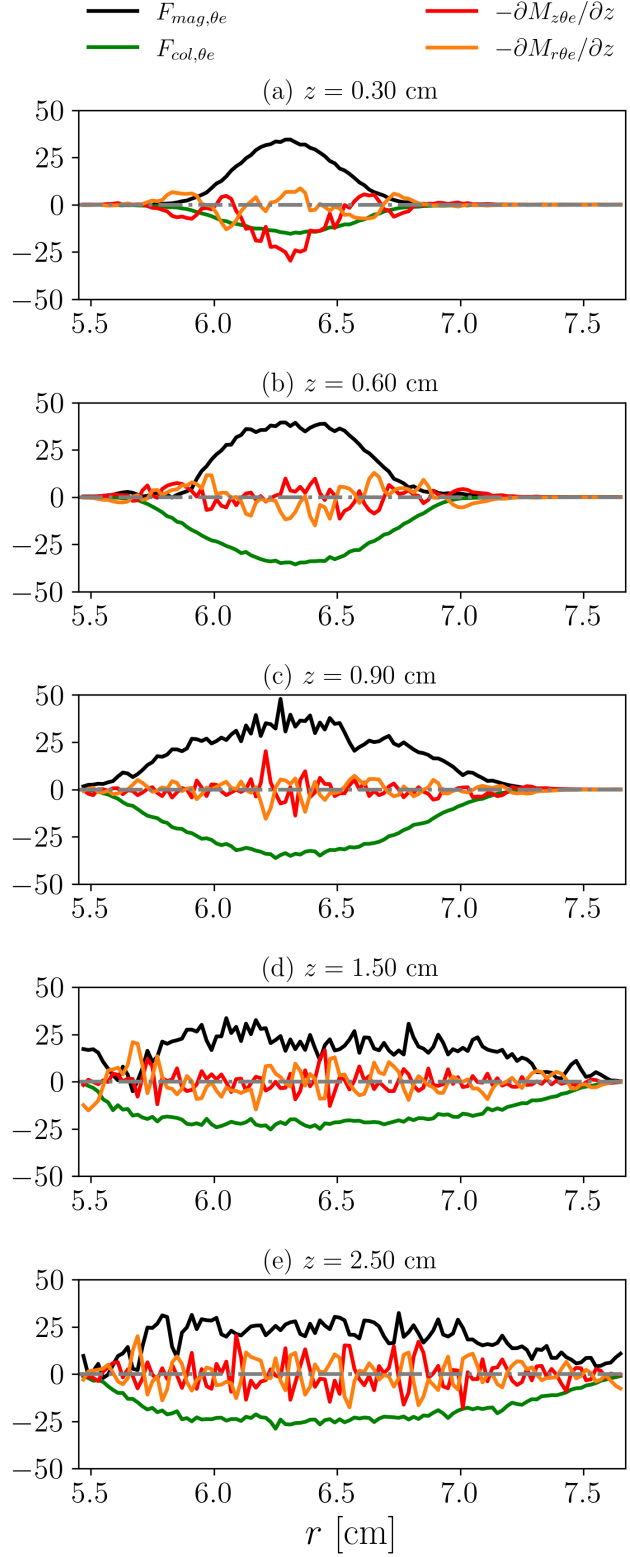


FIG. 26. Main contributions to the axial momentum equation [Eq. (6)] at five different axial sections in N/m³. **AM:** Eliminar

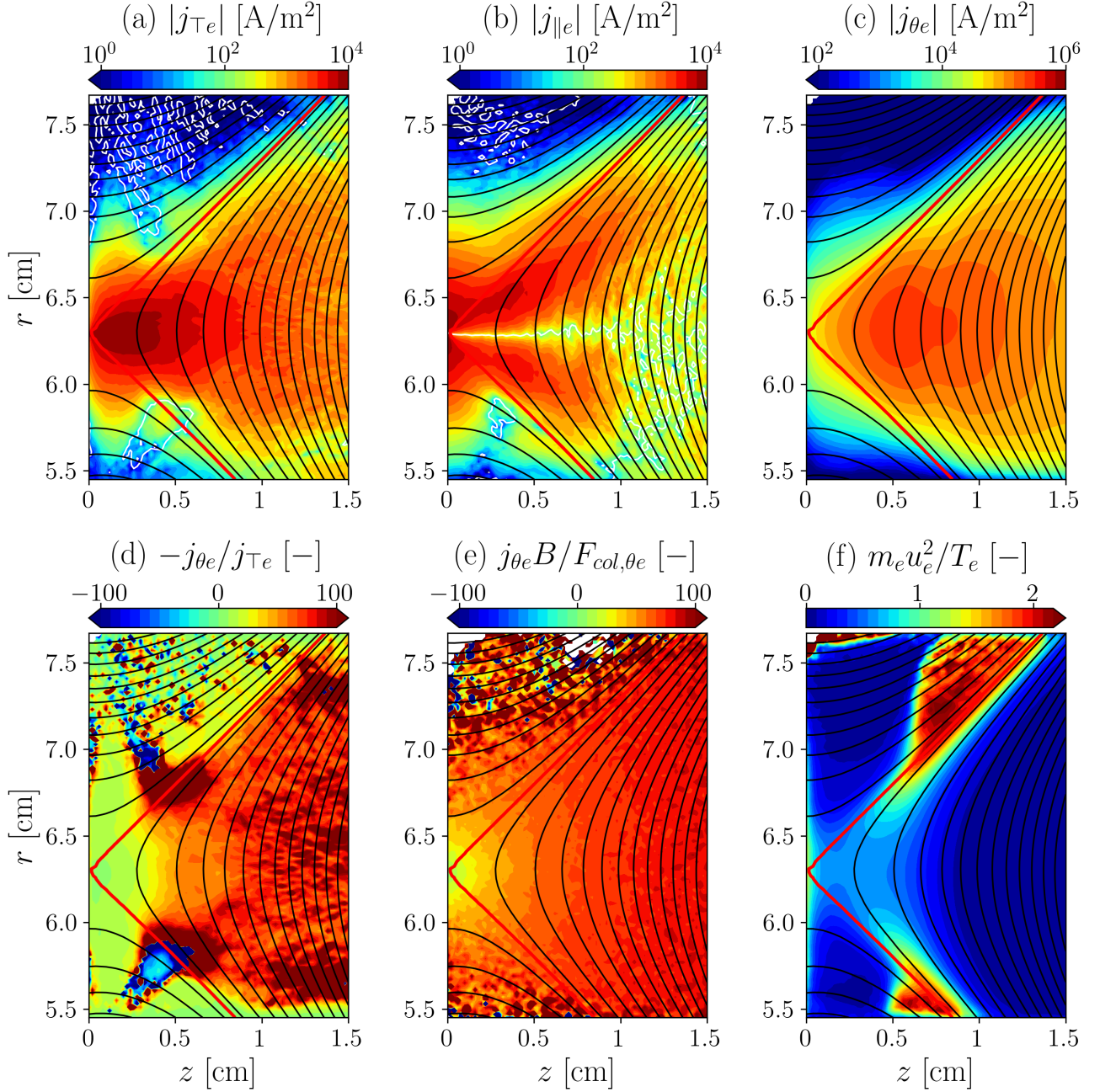


FIG. 27. Other macroscopic plasma variables near the anode: (a) B-perpendicular electron current density, $j_{\perp e}$; (b) B-parallel electron current density, $j_{\parallel e}$; (c) azimuthal electron current density, $j_{\theta e}$; (d) effective Hall parameter, $-j_{\theta e}/j_{\perp e}$; (e) Hall parameter, $j_{\theta e}B/F_{col,\theta e}$; (f) ratio between electron inertia and temperature, $m_e u_e^2/T_e$. **AM: Eliminar**

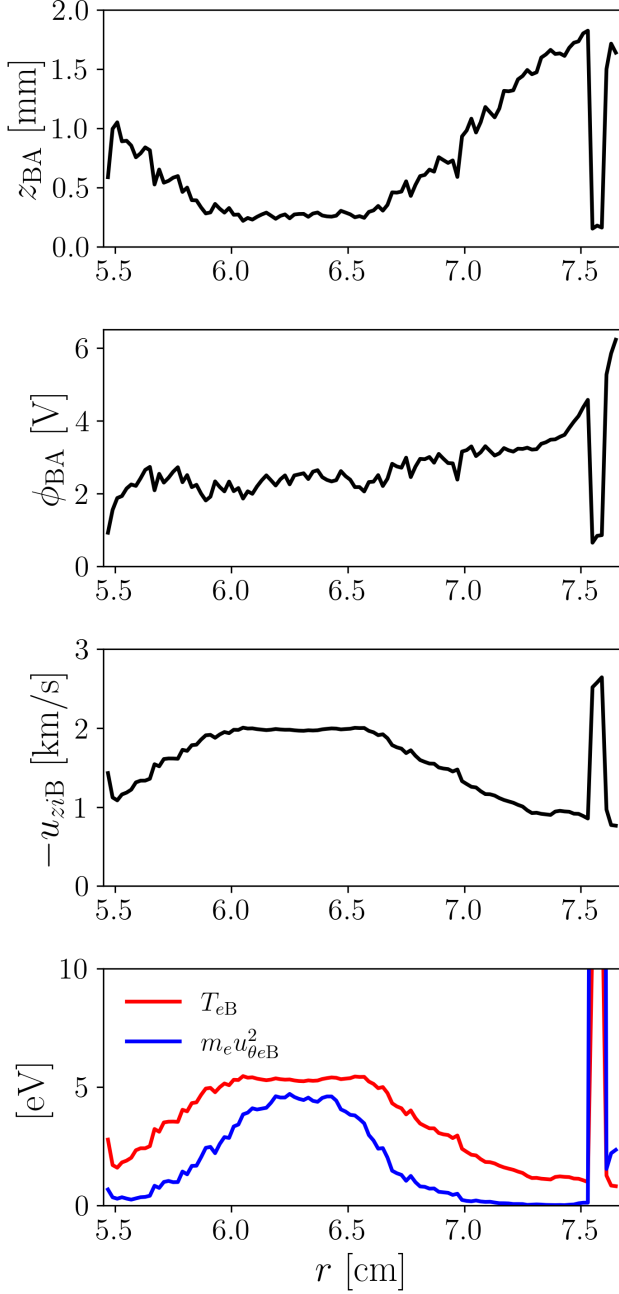


FIG. 28. Anode sheath magnitudes: (a) sheath thickness, z_{BA} ; (b) sheath potential drop, ϕ_{BA} ; (c) axial ion velocity at the sheath edge, $-u_{ziB}$; and (d) electron temperature and azimuthal inertia at the sheath edge, T_{eB} and $m_e u_{\theta eB}^2$, respectively. The sheath edge, B, is considered to be at the location where ions become sonic, $-u_{zi} = \sqrt{T_e/m_i}$.